



Eidgenössische Technische Hochschule Zürich
Swiss Federal Institute of Technology Zurich

Emulating baryon effects on the power spectrum of the cosmological matter density field

MASTER THESIS

Nicola Stoirà

April 2019

Supervised by Dr. Aurel Schneider

Prof. Dr. Alexandre Refregier, Dr. Adam Amara

Cosmology Research Group, Department of Physics, ETH Zurich

Abstract

Weak lensing observables are subject of uncertainty due to the poorly understood physics related to the effects of baryonic feedback on the matter density distribution. In order to get more accurate constraints on the standard cosmological model, it is important to develop new tools to accurately describe the effects of the presence of baryons around dark matter halos. Starting from gravity-only N -body simulations, which describe the distribution of dark matter particles neglecting baryonic effects, we construct an emulator that mimics the power suppression of the matter power spectrum. The emulator is a fast and accurate tool which performs within 1.5% error at 1σ -level. Its construction is based on a *baryonic correction model* (Schneider et al. 2019) which modifies the halo profiles by adding components related to gas and stars. We show that the only cosmological dependence of the model resides in the cosmic fraction $f_b = \Omega_b/\Omega_m$. According to this model we displace the outputs of N -body simulation and we calculate the power suppression. The emulator is constructed on a set of power suppression data by implementing the metamodeling technique called polynomial chaos expansion. Consequently, we implement our emulator into the integrated cosmological Boltzmann solver **PyCosmo** in order to calculate the angular power spectrum. We compare our results with alternative methods and we conclude that X-ray observations have the potential to put strong priors on baryonic feedback scenarios.

Contents

1	Introduction	1
2	Probing baryon effects	2
2.1	Baryonic correction model	2
2.1.1	Background	2
2.1.2	Stellar profile	3
2.1.3	Gas profile	3
2.1.4	Collisionless matter profile	4
2.1.5	Validity of the baryonic correction model	4
2.2	Matter power spectrum suppression	4
2.2.1	Construction of the suppression parameter	4
2.2.2	Cosmology dependence	5
2.2.3	Defining a reference N -body simulation	7
3	Emulator of baryon effects	8
3.1	Emulator configuration	8
3.1.1	Experimental design	8
3.1.2	Emulator construction	9
3.1.3	Choice of the best emulator configuration	10
3.2	Emulator performance	11
4	Baryonic corrections on the shear angular power spectrum $C(\ell)$	18
4.1	$C(\ell)$ construction and comparison	18
4.1.1	Construction and implementation	18
4.1.2	Reference baryonic models	19
4.1.3	Fitting function for the baryon feedback effects	19
4.1.4	Modified halo-model accounting for baryon feedback effects	20
4.1.5	Comparison of the baryonic models	20
4.2	Power suppression of the angular power spectrum spectrum	22
4.2.1	Angular power spectrum suppression for the reference models	22
4.2.2	Angular power spectrum suppression dependence on baryonic parameters	23
5	Conclusion	25

1 Introduction

The Λ Cold Dark Matter (Λ CDM) model is nowadays accepted as the standard model of cosmology. The model consists mainly of two mysterious component: dark matter and dark energy. The nature of these components has not yet been established and remains one of the most pressing questions in cosmology. Ongoing research aims to find confirmations for or against the current cosmological model. In this respect, it is of vital importance to exploit a variety of cosmological probes that can accurately put constraints on it.

Key tools for the study of the distribution of matter in the Universe are galaxy and weak lensing surveys. Current surveys like KiDS¹, HSC², DES³, and upcoming survey like LSST⁴, Euclid⁵, and WFIRST⁶ will contribute to our understanding of the Universe. Nevertheless, observations alone are not sufficient to constrain the standard model of cosmology. In fact, theoretical predictions are necessary and when compared to actual observations they can put restriction on the cosmological parameters. Nowadays, weak lensing measurements are affected by uncertainties related to the poor understanding of the baryonic processes influencing the total matter distribution. As a consequence, baryonic feedback like active galactic nuclei feedback, star formation, and radiative cooling can affect measurements of cosmological parameters, and must therefore be included into theoretical predictions of the weak lensing signal in order to take full advantage of the results of present and future weak lensing surveys.

The weak lensing signal depends on the growth of the matter density field in the Universe. A useful tool for the study of the growth of structure is the matter power spectrum. It is a convenient statistics to measure the clustering amplitude of matter as a function of scale. Through the redshift parameter z , it characterise cosmological structure at different cosmic epochs therefore tracing their evolution. Full-gravity numerical simulations (e.g. [18]) are implemented to accurately describe the level of clustering on different scales. However, these N -body simulations are based exclusively on dark matter and therefore neglect the effects that baryons have on the matter distribution. It has been predicted (e.g. [23]), that both the matter power spectrum and the weak lensing angular power spectrum are affected by beyond percent power suppression due to baryonic feedback effects.

Recently, several studies focused on baryonic corrections of the matter power spectrum (e.g. [5, 16, 23]). In particular, Ref. [23] presents a *baryonic correction model* based on a corrected halo profile which accounts also for star and gas components, in addition to the dark matter component. N -body simulation outputs are then displaced according the corrected profile in order to mimic baryonic influence on the matter density field.

In this paper, we construct an emulator that mimics the baryonic power suppression of the matter power spectrum at medium and small cosmological scales. The basis of this emulator lies in the *baryonic correction model* developed by Schneider et al. [23]. The model has five free parameters, two related to the stellar profile ($\eta_{\text{star}}, \eta_{\text{cga}}$) and three related to the gas profile ($M_c, \mu, \theta_{\text{ej}}$). The emulator consists in a fast and accurate interpolation tool which can be used to scan the parameter space. The final product is a user-friendly instrument which could be implemented to test the results of hydrodynamical simulations. Consequently, we implement the emulator for the calculation of the weak lensing shear angular power spectrum. The final product is a new method to calculate this observable quantity which can be used to perform a full cosmological parameter estimate that accounts for baryonic corrections.

This paper is structured as follows. In Section 2, we summarise the baryonic correction model (Schneider et al. [23], 2018) and its matter components. Moreover, we introduce the concept of matter power spectrum, we describe the power suppression related to the presence of baryons, and we test its dependence on cosmological parameters. In Section 3, we describe the construction of the baryon effects emulator and we test its performance through different error estimation methods. In Section 4, we introduce the concept of the weak lensing shear angular power spectrum and we compare our implementation, based on our emulator, with several alternative models described in the literature. Moreover, we consider the power suppression of the angular power spectrum due to baryon feedback effects, and we test its dependence on the baryonic model free parameters.

¹<http://kids.strw.leidenuniv.nl>

²<https://hsc.mtk.nao.ac.jp/sssp>

³<https://www.darkenergysurvey.org>

⁴<https://www.lsst.org>

⁵<https://www.euclid-ec.org>

⁶<https://wfirst.gsfc.nasa.gov>

2 Probing baryon effects

The matter power spectrum is a convenient statistics to measure the clustering amplitude of structure in the Universe as a function of scale. It can be measured at different epochs by considering different redshifts z . N -body simulations are numerical tools implemented to solve the equations of motion of a system of N particles in order to quantify the evolution of the cosmic density field. Current N -body simulations consider only the gravitational interactions between dark matter particles and therefore they do not take into account the presence of baryons in the centre of dark matter halos and their effects on the total density field. It is therefore important to account for these baryonic effects, which affect the distribution of matter at medium and small cosmological scales, in order to have an accurate description of the cosmic density field. Its modification leads to variations of the clustering amplitudes, which are quantified by measuring the matter power spectrum.

In this section we introduce the theory and the tools needed to study the baryonic effects on the matter power spectrum. In Section 2.1 we present an overview of the baryonic correction model which introduces a dark-matter-baryon (dmb) profile as a substitute for the dark-matter-only (dmo) profile. In Section 2.2 we describe the power suppression, given by the ratio between dmo- and dmb-power spectrum, its dependence on cosmological parameters and we define a reference N -body simulation for further purposes.

2.1 Baryonic correction model

In Section 2.1.1 we introduce the basics of the baryonic correction model (BCM). In Sections 2.1.2, 2.1.3, and 2.1.4 we describe the stellar, the gas, and the collisionless component of the corrected profile. For a more detailed and complete description of the model refer to Schneider et al. [21, 23].

2.1.1 Background

The aim of the baryonic correction model is to account for baryonic effects on the total density field of dark-matter-only N -body simulations. It replaces the dark matter halo profile, that can be described by a truncated NFW profile $\rho_{\text{nfw}}(r)$ and a 2-halo density component $\rho_{2\text{h}}(r)$

$$\rho_{\text{dmo}}(r) = \rho_{\text{nfw}}(r) + \rho_{2\text{h}}(r), \quad (1)$$

with multiple terms accounting for the baryonic effects

$$\rho_{\text{dmb}}(r) = \rho_{\text{gas}}(r) + \rho_{\text{cga}}(r) + \rho_{\text{clm}}(r) + \rho_{2\text{h}}(r). \quad (2)$$

The density profile $\rho_{\text{dmb}}(r)$ is called dark-matter-baryon (dmb) halo density profile. It is composed by $\rho_{\text{gas}}(r)$ which describes the gas contained in the halo, $\rho_{\text{cga}}(r)$ which represents the density profile of the bright galaxy in the halo centre, $\rho_{\text{clm}}(r)$ which describes the collisionless matter composed mainly of dark matter but also of satellite galaxies and unbound stars, and $\rho_{2\text{h}}(r)$ that considers the fact that halos are mostly situated in high-density regions.

In order to mimic the effects of baryons on the matter power spectrum we implement the baryonic correction model on the output of N -body simulations. We achieve this task by implementing the `corforb` code developed by Schneider A. [22]. The code takes as input one N -body simulation output and, according to a specific displacement function (Eq.3), it displaces all the simulation particles around halos such that the total density field recover the profile $\rho_{\text{dmb}}(r)$ from the original profile $\rho_{\text{dmo}}(r)$. The displacement function

$$d(r_{\text{dmo}}|M, c) = r_{\text{dmb}}(M) - r_{\text{dmo}}(M) \quad (3)$$

is defined for every halo mass M and concentration c . Due to this dependence, the radial displacement of particles in different halos changes.

The baryonic correction model has five free parameters M_c , μ , θ_{ej} , η_{star} , and η_{cga} . In the following three sections, we describe the additional matter components introduced in Eq.2 and we give the definition and the role of each of those free parameters.

2.1.2 Stellar profile

One component of the dark-matter-baryon profile is related to the presence of stars in the halo. In particular, $\rho_{\text{cga}}(r)$ describes the bright galaxy in the halo centre through an exponentially truncated power-law profile,

$$\rho_{\text{cga}}(r) = \frac{f_{\text{cga}}}{4\pi^{3/2}} \frac{M_{\text{tot}}}{R_{\text{h}}} \frac{1}{r^2} \exp \left[- \left(\frac{r}{2R_{\text{h}}} \right)^2 \right], \quad R_{\text{h}} = 0.015r_{200} \quad (4)$$

where f_{cga} represents the abundance of stars in the central galaxy, M_{tot} is the total halo mass, R_{h} is the stellar half-light radius, and r_{200} is the virial radius of the halo, i.e. $\rho(< r_{200}) = 200\rho_{\text{crit}}$ such that $M_{200} = \frac{4}{3}\pi\rho_{\text{crit}}r_{200}^3$. The profile $\rho_{\text{cga}}(r)$ is motivated by the study of galaxy clusters. In this respect, stellar masses are measured accurately through optical and infrared observations, whereas total masses of clusters are derived from X-ray observations [23].

The total stellar fraction is formed by the stars in the central galaxy f_{cga} and the satellite population f_{sga} , i.e. $f_{\text{star}} = f_{\text{cga}} + f_{\text{sga}}$. The stellar fractions are parametrised by

$$f_{\text{star}}(M_{200}) = A \left(\frac{M_1}{M_{200}} \right)^{\eta_{\text{star}}}, \quad f_{\text{cga}}(M_{200}) = A \left(\frac{M_1}{M_{200}} \right)^{\eta_{\text{cga}}}. \quad (5)$$

with $A = 0.09$, $M_1 = 2.5 \times 10^{11} M_{\odot}/h$, and $\eta_{\text{star}} < \eta_{\text{cga}}$, i.e. $f_{\text{star}} > f_{\text{cga}}$ [23]. These functional forms have been compared to abundance matching results from the literature [23]. The free parameter η_{cga} then characterises the stellar fraction of the central galaxy and the free parameter η_{star} characterises the total stellar fraction within a halo, comprising central galaxy, satellite galaxies and halo stars. However, it has to be clarified that the satellite population is not included in the stellar profile because it is considered as collisionless and so is described by the collisionless matter profile in Section 2.1.4.

2.1.3 Gas profile

The gas profile $\rho_{\text{gas}}(r)$ is the most important component for the baryonic corrections on the matter power spectrum. Its parametrisation is motivated by stacked X-ray observations from ROSAT/PSPC⁷ and XMM-Newton⁸ [23]. The gas profile is parametrised by

$$\rho_{\text{gas}}(r) = \frac{\rho_{\text{gas},0}}{(1+u)^{\beta}(1+v^2)^{(7-\beta)/2}}, \quad (6)$$

with $u = r/r_{\text{co}}$ and $v = r/r_{\text{ej}}$. The gas profile has three main characteristics: a central core with core radius r_{co} , a power-law decrease of slope β , and a truncation set by the maximum gas ejection radius r_{ej} . The central core radius (r_{co}) of the profile is defined by the relation

$$r_{\text{co}} = \theta_{\text{co}}r_{200}, \quad (7)$$

where the core parameter is fixed to $\theta_{\text{co}} = 0.1$ which is in agreement with observations of X-ray profiles, e.g. from XMM-Newton and Chandra⁹ [23]. The maximum gas ejection radius (r_{ej}) is defined by

$$r_{\text{ej}} = \theta_{\text{ej}}r_{200} \quad (8)$$

and establishes the region beyond which the gas density decreases analogously to the truncated NFW profile. In particular, the free parameter θ_{ej} specifies the maximum radius of gas ejection in comparison to the virial radius. The normalisation parameter $\rho_{\text{gas},0}$ depends on the gas fraction $f_{\text{gas}} = \Omega_{\text{b}}/\Omega_{\text{m}} - f_{\text{star}}$ and it is defined in Eq. 2.13 in [23].

In agreement with X-ray observations, the slope β of the gas density profile $\rho_{\text{gas}}(r)$ depends on the halo mass and is described by

$$\beta(M_{200}) = 3 - \left(\frac{M_{\text{c}}}{M_{200}} \right)^{\mu}, \quad (9)$$

⁷www.dlr.de/en/rosat

⁸<http://xmm.esac.esa.int>

⁹<http://chandra.harvard.edu/>

where the free parameter M_c defines the characteristic mass scale at which β starts to deviate substantially from $\beta = 3$ towards small halo masses, and the free parameter μ defines the rate of decrease of the slope towards small halo masses. The slope is restricted to $\beta \leq 3$, meaning that the gas profile can not be steeper than the NFW profile. This parameter is especially important because it quantifies the amount of gas pushed out beyond the virial radius.

2.1.4 Collisionless matter profile

Apart from dark matter which is the major collisionless component, the collisionless matter profile also accounts for the satellite population of stars. This is not the case in gravity-only simulations, which model the collisionless matter component as a NFW profile. Stars and gas inside halos influence gravitationally the collisionless matter leading to two possible scenarios of the so called adiabatic relaxation, i.e. adiabatic contraction or adiabatic expansion. Therefore, the collisionless matter profile reacting to the presence of stars and gas is described by

$$\rho_{\text{clm}}(r) = \frac{f_{\text{clm}}}{4\pi r^2} \frac{d}{dr} M_{\text{nfw}}(r/\zeta), \quad f_{\text{clm}} = \Omega_{\text{dm}}/\Omega_{\text{m}} + f_{\text{sga}}, \quad (10)$$

where M_{nfw} is the mass profile of a truncated NFW profile and $\zeta = r_f/r_i$ is the ratio of the radii after (dmb-profile) and before (dmo-profile) adiabatic relaxation caused by the presence of baryonic matter inside the halo [23].

2.1.5 Validity of the baryonic correction model

The validity of the baryonic correction model is compared in [23] with the results of hydrodynamical simulations. In particular, they compare the model with the results from OWLS (Over- Whelmingly Large Simulation) [20]. They find that the agreement between the matter power spectrum of the baryonic correction model and the results from hydrodynamical simulations is better than two percent at $z = 0$, four percent at $z = 1$, and ten percent at $z = 2$ considering cosmological scales up to $k = 10 \text{ h/Mpc}$. So, the model works quite well at redshift $z = 0$, and it degrades towards higher redshifts, but this is due to the setup of the model parameters according to simulated gas fractions at redshift $z = 0$.

2.2 Matter power spectrum suppression

The effects of baryons on the matter power spectrum at medium and small cosmological scales plays a central role in our study. We study it by defining a matter power spectrum suppression parameter $B(k, z) = P_{\text{dmb}}(k, z)/P_{\text{dmo}}(k, z)$. The suppression parameter is constructed on a dmo-power spectrum P_{dmo} from an underlying N -body simulation output and a corrected power spectrum P_{dmb} from the displaced simulation output constructed on a chosen baryonic correction model.

2.2.1 Construction of the suppression parameter

We are interested in calculating the matter power spectrum suppression for given cosmological and baryonic correction model parameters. In this section we summarise the procedure to derive this quantity.

First we need a reference N -body simulation based on a cosmology with given parameters Ω_{m} , $\Omega_{\text{b}}h^2$, h , n_{s} , and σ_8 . We run the simulations using the code PKDGRAV3 developed by Potter et al. [18]. This code is a fast multipole method that has been used to simulate up to 8 trillion particles. With this code we measure the matter power spectrum of the simulation outputs.

Secondly, we choose a combination of the baryonic parameters M_c , μ , θ_{ej} , η_{star} , and η_{cga} , and we implement `corforb` to displace the particles of the dark-matter-only results. In order to modify the halo profiles and displace the particles, the code requires a specific halo catalogue for each N -body simulation performed. These catalogues are generated by means of the AMIGA'S HALO FINDER (AHF) [4, 9]. Based on a cosmological simulation, this halo finder is able to find halo centres, collect particles bound to them and remove unbounded particles, and calculate various halo properties. Once this is done, we calculate, similarly as for the dark-matter-only case, the matter power spectrum of the displaced simulation output.

Finally, we simply take the ratio of the corrected power spectrum over the dark-matter-only-power spectrum.

In Sections 2.2.2 and 2.2.3 we show that this process can be simplified by considering the cosmological dependence of the matter power spectrum suppression and by defining a reference simulation for all input cosmologies.

2.2.2 Cosmology dependence

In this section we investigate the cosmology dependence of the suppression parameter $B(k, z)$. We study the influence of five cosmological parameters: the matter density Ω_m , the baryon density $\Omega_b h^2$, the Hubble parameter h , the spectral index n_s , and σ_8 (which describes the power spectrum amplitude on the scale of 8 Mpc/ h). As reference we assume a Λ CDM concordance cosmology described in Table 1 [17].

Ω_m	$\Omega_b h^2$	h	n_s	σ_8
0.315	0.0224	0.674	0.965	0.811

Table 1: Λ CDM concordance cosmology which we use as reference cosmology throughout the document. The parameters are given by the latest result from the Planck Collaboration [17].

We are interested on medium cosmological scales on which the baryonic effects, due to the feedback effects pushing the gas out of the halos, lead to a power suppression. The dark-matter-baryon power spectrum P_{dmb} is constructed on a fixed baryonic correction model described in Table 2.

M_c	μ	θ_{ej}	η_{star}	η_{cga}
1×10^{14}	0.4	4.0	0.3	0.6

Table 2: Reference baryonic model.

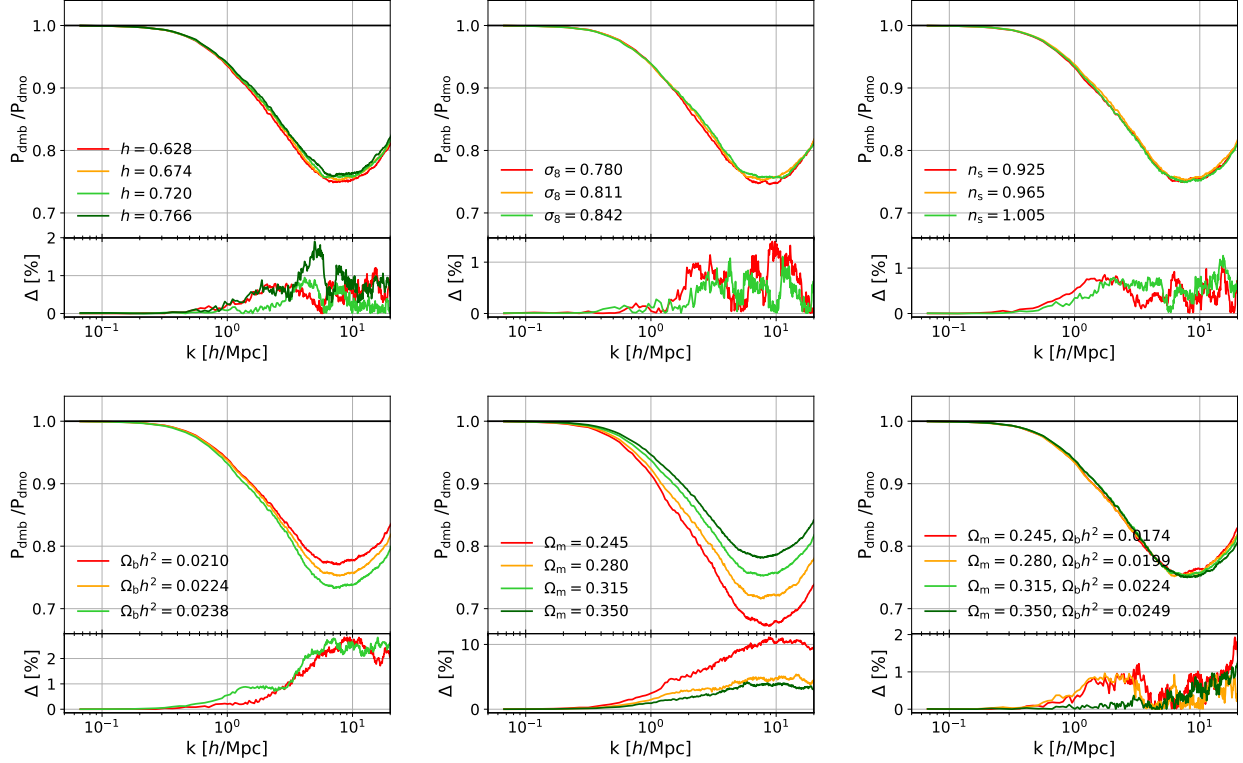


Figure 1: Cosmology dependence of the baryon suppression based on a fixed baryonic correction model with $M_c = 1 \times 10^{14}$, $\mu = 0.4$, $\theta_{ej} = 4.0$, $\theta_{co} = 0.1$, $\eta_{star} = 0.3$, and $\eta_{cga} = 0.6$. *Top from left:* dependence on Hubble parameter h , dependence on σ_8 , and dependence on the spectral index n_s . *Bottom from left:* dependence on the baryon density $\Omega_b h^2$, dependence on the matter density Ω_m , and dependence on the cosmic fraction $f_b = \Omega_b / \Omega_m$. The power spectra are constructed at redshift $z = 0$ on N -body simulations based on the standard cosmology (see Table 1) with only one variable parameter for each case. The simulations have a box size of $L = 128$ Mpc/h and $N = 256$ particles per dimension. The figures on the lower part represent the relative error Δ with respect to the standard cosmology.

For each variation of a cosmological parameter we run a new simulation based on the corresponding cosmology. The cosmology dependence of the power suppression is presented in Fig.1.

In the top-plots of the figure we vary the parameter h , σ_8 , and n_s respectively. We observe a maximum suppression of the order 25% around a scale of $k = 7 - 8$ h/Mpc for all tested parameters. In fact, the power suppression is only slightly influenced by variations of h , σ_8 , and n_s respectively. The deviations from the standard cosmology remain below 1 – 2%, so we conclude that the baryonic effects on the matter power spectrum are not dependent on h , σ_8 , and n_s .

On the other hand, the situations for a variable baryon density $\Omega_b h^2$ (bottom-left) and for a variable matter density Ω_m (bottom-centre) show a stronger dependence. For the baryon density variation, we see that the three cases deviates considerably from each other above scales $k > 3$ h/Mpc, reaching a maximum suppression around $k = 7 - 8$ h/Mpc between 23 – 27%. This deviation is clearly visible and exceeds 2%. For the matter density, we observe that a smaller Ω_m -value implies a larger suppression. In particular, the maximum suppression increases from 22% for a cosmology with $\Omega_m = 0.350$, to 33% for a cosmology with $\Omega_m = 0.245$. The deviation from the standard cosmology is already relevant at large scales with relative errors of 2 – 10%. So, we conclude that the baryonic effects on the matter power spectrum show a clear dependence on the density parameters.

The bottom-right plot considers variable matter and baryon densities by keeping the cosmic fraction fixed to a value of $f_b \approx 0.157$. With this plot we test if the dependence of the baryonic suppression on the density parameters can be described with a single parameter, i.e. the cosmic fraction $f_b = \Omega_b / \Omega_m$. The maximum suppression for all the considered $(\Omega_m, \Omega_b h^2)$ -combinations lies around 25%. So, we observe that the deviations from the standard cosmology remain below 1% at medium cosmological scales indicating that the results are only sensible to the cosmic fraction $f_b = \Omega_b / \Omega_m$ and not to the specific values of matter and baryon density. As a consequence, the effects of variable baryon and matter densities can be described by a

variable cosmic fraction.

Summarising, we conclude that the cosmological dependence of the matter power spectrum suppression due to the presence of baryons is only sensible to the cosmic fraction $f_b = \Omega_b/\Omega_m$. Therefore, we consider f_b as an additional free parameter of the baryonic correction model.

2.2.3 Defining a reference N -body simulation

It is important to test if, for a chosen cosmology, the corresponding N -body simulation is required in order to calculate the power suppression. In terms of computational time needed to calculate the power suppression, using always the same simulation output would be a big improvement. In Section 2.2.2, we have concluded that the matter power spectrum suppression is only sensible to the cosmic fraction f_b . Therefore, we vary only the matter density Ω_m and keep the other cosmological parameters fixed to the standard cosmology (see Table 1).

In Fig.2 we consider the power suppression calculated on four different N -body simulations outputs based on matter densities $\Omega_m = 0.245, 0.280, 0.315, 0.350$. The dark-matter-baryon power spectrum is generated by applying the same correction model on the simulations outputs. The chosen model is equivalent to the standard cosmology with the standard baryonic model defined in Table 2.

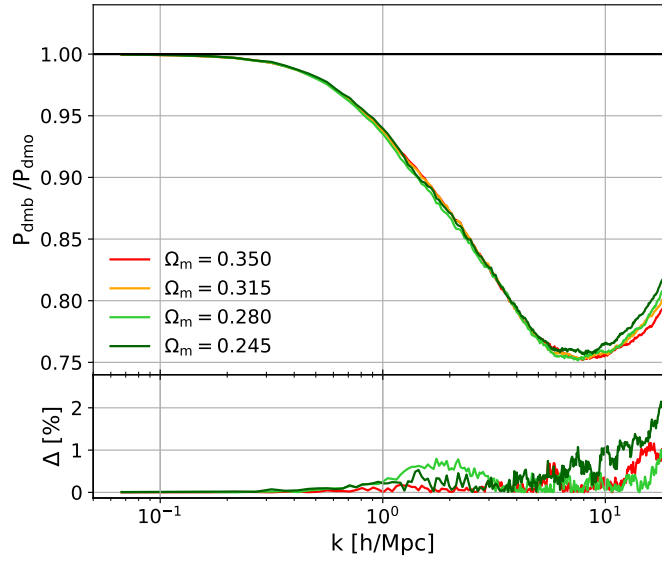


Figure 2: *Top:* power suppression where P_{dmo} is based on N -body simulations with matter densities $\Omega_m = 0.245, 0.280, 0.315, 0.350$ and P_{dmb} is generated from them by applying a baryonic correction model with fixed parameters $\Omega_m = 0.315$, $M_c = 1 \times 10^{14}$, $\mu = 0.4$, $\theta_{\text{ej}} = 4.0$, $\theta_{\text{co}} = 0.1$, $\eta_{\text{star}} = 0.3$, and $\eta_{\text{cga}} = 0.6$. *Bottom:* relative error Δ with respect to the standard cosmology.

The difference between the plot with variable matter density in Fig.1 and Fig.2 is that, in the latter the correction of the dmo-power spectrum assumes a constant matter density $\Omega_m = 0.315$ although the underlying N -body simulations are based on different density values. In the former the corresponding matter density is considered for each simulation. By relating this difference with the comparison of the observed relative errors in both figures (2 – 10% in Fig.1 and < 1 – 2% in Fig.2), we conclude that the large deviations from the standard cosmology, observed in Fig.1, come mostly from the variable matter density used for the displacement of the N -body simulation output and not from the matter density of the underlying simulation itself. Therefore, we conclude that only one reference N -body simulation output is necessary to study the power suppression due to baryonic effects on different cosmologies.

3 Emulator of baryon effects

In this section we describe our emulator approach for the baryon effects on the matter power spectrum. As explained in Section 2.2.1, the calculation of the matter power spectrum suppression requires several steps and some knowledge of the used techniques. Our emulator is a fast and accurate substitute for the calculation of the power suppression at medium and cosmological scales. In order to calculate the power suppression it requires the value of the cosmic fraction $f_b = \Omega_b/\Omega_m$, the baryonic correction parameters M_c , μ , θ_{ej} , η_{star} and η_{cga} , and the redshift z .

Section 3.1 deals with the construction of the emulator. Section 3.2 study its accuracy on a test data set.

3.1 Emulator configuration

This section explains the basic concepts and techniques considered for the construction of an emulator that mimics the baryon effects on the matter power spectrum. The development procedure is inspired by the `EuclidEmulator` presented by Knabenhans et al. in [2].

The emulator is developed in MATLAB using the uncertainty quantification software `UQLab` created by Marelli S. & Sudret B. [13]. It is based on a metamodeling technique called polynomial chaos expansion [14].

3.1.1 Experimental design

The *baryon effects emulator* has six input parameters: f_b , $\log_{10}M_c$, μ , θ_{ej} , η_{star} and η_{cga} . Every combination in the 6-dimensional parameter space generates a different physical environment with its corresponding power spectrum suppression. The parameter space is defined in the following intervals:

$$\begin{aligned} f_b &\in [0.13, 0.21], \\ \log_{10}M_c &\in [12.7, 16.7], \\ \mu &\in [0.1, 1.0], \\ \theta_{ej} &\in [2.0, 8.0], \\ \eta_{star} &\in [0.2, 0.4], \\ \eta_{cga} &\in [0.5, 0.7]. \end{aligned} \tag{11}$$

The ranges for the baryonic parameters are chosen according to the constraints and considerations derived in the work of Schneider et al. [23].

The basis of the emulator is the experimental design (ED). It consists of a set of sample points in the parameter space with the corresponding true evaluation of the matter power spectrum suppression. Each baryonic model is evaluated at five different redshifts $z = \{0, 0.5, 1, 1.5, 2\}$. The ED sample points are generated via the latin hypercube sampling (LHS) [15, 25]. This method aims to pick points that uniformly cover the parameter space. In particular, this method generates samples each of which is the the only one in each axis-aligned hyperplane containing it. We optimise the result by choosing from 10^5 samples, a sample with maximum minimal distance between the sampling points [2]. The ED is chosen by balancing its size, directly related to the accuracy of the emulation, and the computational time required for its construction.

The main goal of the experimental design construction is to find the smallest possible ED that gives the accuracy precision which we aim for, i.e. 1% accuracy. By means of the the software `UQLab` [13] we perform accuracy tests on different ED constructions. Fig.3 presents the average of the highest relative errors $\langle \Delta_{max} \rangle$ as a function of the experimental design size n_{ED} . The accuracy is tested on training data composed by 10 real evaluated sample points. For each of these baryonic models we maximise the relative error over k and take the average of it over all the models. We perform several tests with different restrictions on the model free parameters (Fig.3) in order to find out if they could give a significant advantage in terms of accuracy for small ED sizes.

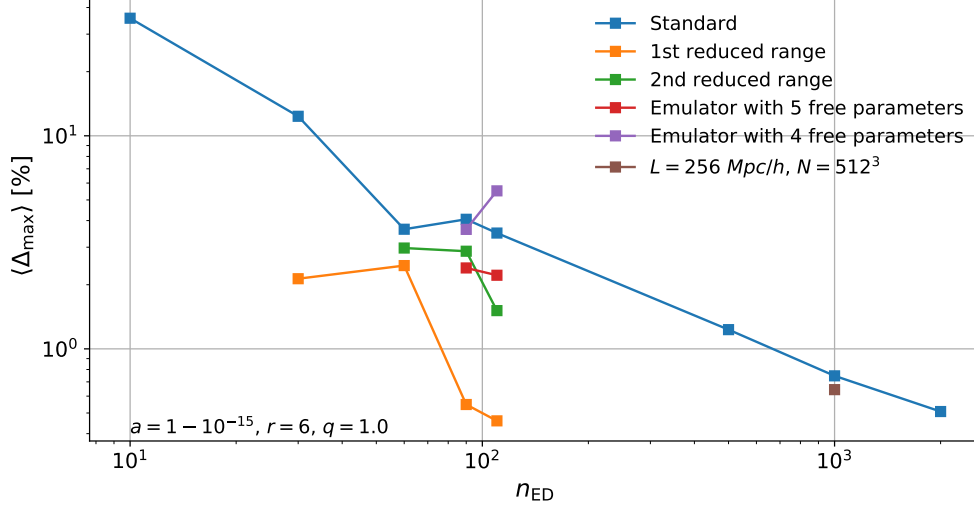


Figure 3: Average of the highest relative errors $\langle \Delta_{\max} \rangle$ as a function of the experimental design size n_{ED} . We use truncation parameters $r = 6$, $q = 1.0$, and accuracy parameter $a = 1 - 10^{-15}$ (Section 3.1.2). *Standard*: emulator constructed on five redshifts and with parameters in the standard ranges of Eq. 3.1.1. *1st reduced range*: free parameters $f_b \in [0.14, 0.17]$, $\log_{10} M_c \in [13.4, 14.6]$, $\mu \in [0.2, 0.6]$, $\theta_{\text{ej}} \in [3.0, 8.0]$, $\eta_{\text{star}} \in [0.2, 0.4]$, and $\eta_{\text{cga}} \in [0.5, 0.7]$. *2nd reduced range*: free parameters $f_b \in [0.13, 0.21]$, $\log_{10} M_c \in [13.0, 15.7]$, $\mu \in [0.15, 0.60]$, $\theta_{\text{ej}} \in [2.2, 6.0]$, $\eta_{\text{star}} \in [0.2, 0.4]$, and $\eta_{\text{cga}} \in [0.5, 0.7]$. *Emulator with 5 parameters*: standard case with θ_{ej} fixed. *Emulator with 4 parameters*: standard case with star components $\eta_{\text{star}}, \eta_{\text{cga}}$ fixed. All those cases are constructed on a small N -body simulation with $L = 128 \text{ Mpc}/h$ and $N = 256^3$. Differently the last case represents the standard emulator but constructed on a larger box with $L = 256 \text{ Mpc}/h$ and $N = 512^3$.

Fig.3 shows that the standard emulators ($L = 128 \text{ Mpc}/h$ and $N = 256^3$), for $n_{\text{ED}} > 1000$, reaches an error smaller than 1%. The results with smaller ranges ($f_b \in [0.14, 0.17]$, $\log_{10} M_c \in [13.4, 14.6]$, $\mu \in [0.2, 0.6]$, $\theta_{\text{ej}} \in [3.0, 8.0]$, $\eta_{\text{star}} \in [0.2, 0.4]$, and $\eta_{\text{cga}} \in [0.5, 0.7]$ and $f_b \in [0.13, 0.21]$, $\log_{10} M_c \in [13.0, 15.7]$, $\mu \in [0.15, 0.60]$, $\theta_{\text{ej}} \in [2.2, 6.0]$, $\eta_{\text{star}} \in [0.2, 0.4]$, and $\eta_{\text{cga}} \in [0.5, 0.7]$), in particular the first case, show a good accuracy for much smaller experimental designs. Nevertheless, we decide to do not consider those cases because the parameter ranges are reduced and we prefer to have a wider choice on the values of the parameters, although this is related to a larger ED and so to higher computational costs.

We conclude that an ED with $n_{\text{ED}} = 1000$ is big enough in terms of required precision. This set of baryonic models and their corresponding evaluated power suppressions is the starting point in the construction of the emulator. Even if it is a rather large ED design containing 5000 evaluations (evaluated at 5 redshifts), the computational costs are sustainable due to the need to run only one N -body simulation per redshift (see considerations on Fig.2). Without this assumption, it would be too expensive in terms of computational time to generate such a large ED.

3.1.2 Emulator construction

In this section we present the operation of the emulator and the several techniques used to develop the final product. For a more detailed description of the used techniques refer to Knabenhans. et al. [2] and Marelli S. & Sudret B. [13, 14].

After the construction of the ED, as described in Section 3.1.1, we have a set of real evaluated suppression parameters for 1000 baryonic models at different redshifts z and scales k . We store the logarithm of the ED evaluations in a $n_{\text{ED}} \times (n_z \cdot n_k)$ data matrix \mathbf{D} . We take the logarithm of the suppression parameter because, analogously to the results of [2], it gives a higher accuracy. Using the uncertainty quantification software UQLab we decompose this data matrix.

Firstly we perform a principal component analysis (PCA) that separates the baryonic parameters dependence from the wavenumber k and the redshift z . The data matrix is decomposed in principal components

$$\mathbf{D} = \sum_{i=1}^{n_{\text{ED}}} \lambda_i(f_b, M_c, \mu, \theta_{\text{ej}}, \eta_{\text{star}}, \eta_{\text{cga}}) \text{PC}_i(k, z). \quad (12)$$

The final number of principal components n_{PCA} that is considered depends on the size of the experimental design n_{ED} and on the accuracy parameter a (see below).

Secondly, we perform a polynomial chaos expansions (PCE; metamodeling technique that uses spectral representation constructed on a basis of polynomial functions to provide a functional approximation of a computational model; [14]) on the coefficients λ_i of the PCA

$$\lambda_i(f_b, M_c, \mu, \theta_{\text{ej}}, \eta_{\text{star}}, \eta_{\text{cga}}) \approx \sum_{\alpha \in \mathcal{A}} \gamma_\alpha \Psi_\alpha(\mathbf{x}), \quad (13)$$

where $\alpha = (\alpha_1, \dots, \alpha_6)$ represents a multi-index, Ψ_α the polynomial basis element and γ_α its corresponding coefficient [2, 14]. The polynomial basis elements $\Psi_\alpha(\mathbf{x})$ are defined by a set of normalized Legendre polynomials

$$\Psi_\alpha(\mathbf{x}) = \phi_{\alpha_1}(x_1) \dots \phi_{\alpha_6}(x_6) = \prod_{l=1}^6 \sqrt{2\alpha_l + 1} P_{\alpha_l}(x_l), \quad (14)$$

where $\mathbf{x} = (x_1, \dots, x_6)$ refers to the six free parameters of the model mapped to the interval $[-1, 1]$. The set of selected multi-indices of multivariate polynomials, $\mathcal{A} \subset \mathbb{N}^6$, is restricted by truncation schemes. Maximum interaction truncation – parametrized with r – allows the α 's to have at most r non-zero elements, and can be used to limit the interaction terms. Hyperbolic truncation – parametrized with q – includes all the high-degree terms in each single variable, but discourages equivalently high order interaction terms [14]. According to those truncation schemes we get a restricted set of selected multi-indices

$$\mathcal{A}' = \left\{ \alpha \in \mathbb{N}^6 : \left(\sum_{i=1}^6 \alpha_i^q \right)^{1/q} \leq p, \quad \sum_{i=1}^6 \mathbf{1}_{\{\alpha_i > 0\}} \leq r \right\}, \quad (15)$$

where p is the maximal total degree of polynomials.

Finally we use the least angle regression-based selection (LARS) algorithm [1, 14] for the calculation of the PCE coefficients γ_α . This method determines an optimal set of polynomials $\mathcal{A} \subset \mathcal{A}'$ consequently implemented in the truncated series in Eq.13.

The steps described above can be performed in MATLAB with the use of UQLab-packages. The final result is a numerical model that contains all the important quantities introduced above. We can then define six values of the free parameters and, with the UQLab function `uq_evalModel()`, we can evaluate the model at the chosen point in the parameter space.

3.1.3 Choice of the best emulator configuration

In Sections 3.1.1 and 3.1.2 we motivate the choice of the experimental design size $n_{\text{ED}} = 1000$, and we respectively describe the technical processes used to construct the emulator. In this section we generate multiple emulators based on different accuracy and truncation parameters combinations (a, r, q) in order to find the most accurate configuration. The results of this study are similar for the emulator based on small ($L = 128 \text{ Mpc}/h$, $N = 256^3$) and large ($L = 256 \text{ Mpc}/h$, $N = 512^3$) N -body simulations. Due to computational costs, less (a, r, q) -combinations are tested for the larger box. Nevertheless, we consider the results for larger N -body simulations because the final result is smoother and more precise.

As introduced in the previous section the accuracy parameter a defines, together with the n_{ED} , the number of principal components n_{PCA} . If a increases towards 1, then the number of PC increases towards n_{ED} leading to a computational time increment. We define $a = 1 - 10^{-\chi}$, and for the best emulator search we consider $\chi = 3, 4, 5$. We allow the maximum interaction r to take the following values $r = 2, 3, 4, 5, 6$. On the other hand, for the hyperbolic truncation scheme we consider $q = 0.1, 0.2, \dots, 1.0$.

Before creating an emulator for each of the 150 possible (a, r, q) -combinations, we define a training set of reference sample points in the 6D-parameter space. We consider six training points, outside of the ED, generated by means of the LHS technique [15, 25]. The emulation of those points is compared to the real result in order to test the accuracy of each emulator. For every (a, r, q) -combination we generate an emulator and for each of those emulators we calculate the relative error over all the k -values and we take the

maximum of it for every sample point considered. Then we take the maximum over all the sample points for each emulator (cross validation error). In the end, we have a value assigned to each (a, r, q) -combination that represents the highest relative error tested on the training sample points. Finally, the best emulator is found by simply choosing the one that has the smallest value for the highest relative error.

The best combination found is given by the following accuracy and truncation parameters

$$a = 1 - 10^{-5} (n_{\text{PCA}} = 24) \quad r = 4 \quad q = 0.6 \quad (16)$$

with a maximum relative error of about 0.68%. This is the final configuration of the *baryon effects emulator*. Of course, we do not expect to always find errors below 0.68% because we have tested its operation only on 6 sample points. Nevertheless, we are confident that this is an accurate configuration for the description of the parameter space.

3.2 Emulator performance

In Section 3.1 we describe the construction of the *baryon effects emulator* and we define a combination of n_{ED} , a , r , and q representing the best performance. In particular, the best choice is given by $n_{\text{ED}} = 1000$, $a = 1 - 10^{-5}$, $r = 4$, and $q = 0.6$. In this section we test the accuracy of this emulator at different redshifts $z = \{0, 0.234, 0.5, 0.767, 1, 1.281, 1.5, 1.798, 2\}$ on a test data set composed of six sample points outside of the ED. It is important to emphasise that, in order to have a reliable accuracy estimation, the test data set is different from the training set used to construct the best emulator in Section 3.1.3. Table 3 describes the six sample points chosen, which are generated with the LHS method [15, 25]. Each of this points represents a different baryonic model in a Universe with a different cosmic fraction $f_b = \Omega_b/\Omega_m$. As described in the considerations concerning Fig.2, the power suppression is only sensible to the cosmic fraction. This means that a specific f_b -value can be interpreted as several physical situations with different Ω_m and Ω_b .

	f_b	$\log_{10} M_c$	μ	θ_{ej}	η_{star}	η_{cga}
Sample 0	0.207046862	16.6008945	0.172824341	3.30837966	0.314065654	0.568866902
Sample 1	0.171753000	15.1972851	0.938900789	5.10189264	0.370061019	0.555513395
Sample 2	0.131911086	13.5288144	0.339449947	6.60468011	0.360097111	0.624989236
Sample 3	0.185102187	14.4185415	0.498056100	2.00671323	0.267163204	0.679916413
Sample 4	0.149839396	15.9845697	0.797082016	7.35391483	0.209096312	0.637623288
Sample 5	0.162102650	12.8009277	0.582857882	4.13550454	0.236488679	0.531574004

Table 3: Test data sampled from the 6D-parameter space using the latin hypercube sampling technique.

In order to have a complete tool to calculate the baryonic corrections, we have developed a short `python` code [24] (development inspired by the work of Knabenhans M. [8]) constructed on the previously generated model (Section 3.1.2). As input it requires a vector containing redshifts $z \in [0, 2]$, an optional k -vector for the evaluation positions, and the emulator free parameters described in Section 3.1.1. The output, calculated in about a second, contains the k -values of evaluation and the corresponding suppression parameter values for every input redshift. As explained in Section 3.1.1, the experimental design is constructed on five redshifts $z \in \{0, 0.5, 1, 1.5, 2\}$. The choice of an arbitrary redshift z is made possible by a linear interpolation of the results of the nearby defined redshift values.

By means of this code, we can emulate the power suppression for the sample points described in Table 3. In the figures 4,5,6,7,8,9, the upper part shows the real evaluated ratio $P_{\text{dmb}}/P_{\text{dmo}}$ (continuous lines) and the results from the baryon effects emulator (dashed lines). The lower part represents the generalized error between emulation and real evaluation. In each of those figures, the plot on the left describes the redshift values $z \in \{0, 0.5, 1, 1.5, 2\}$ on which the ED is constructed (we refer to them as standard redshifts), and the plot on the right describes four linearly interpolated redshifts $z \in \{0.234, 0.767, 1.281, 1.798\}$ (we refer to them as interpolated redshifts). We anticipate that the emulation of the test points is not always as accurate as expected. Nevertheless, the highest relative error remains restricted to a 3.3% margin (Figs.4, 10).

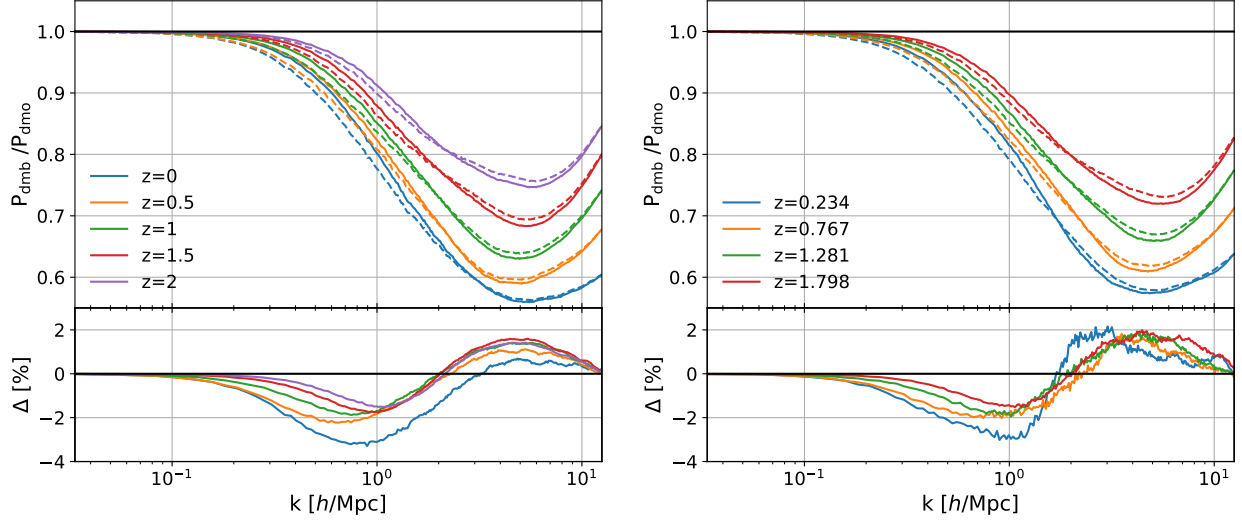


Figure 4: Results for the emulation of sample 0: $f_b = 0.207046862$, $\log_{10} M_c = 16.6008945$, $\mu = 0.172824341$, $\theta_{ej} = 3.30837966$, $\eta_{star} = 0.314065654$, and $\eta_{cga} = 0.568866902$.

The baryonic model of sample 0, shown in Fig.4, has the highest relative error. The emulation follows the shape of the real data, but around $k = 1 \text{ h/Mpc}$ and $k = 5 \text{ h/Mpc}$ the former deviates significantly from the latter. The results for the interpolated redshifts reflect the errors that affect the standard ones. The matter power spectrum suppression for this baryonic model is more suppressed at redshift $z = 0$ by almost 45% around $k = 5 - 6 \text{ h/Mpc}$.

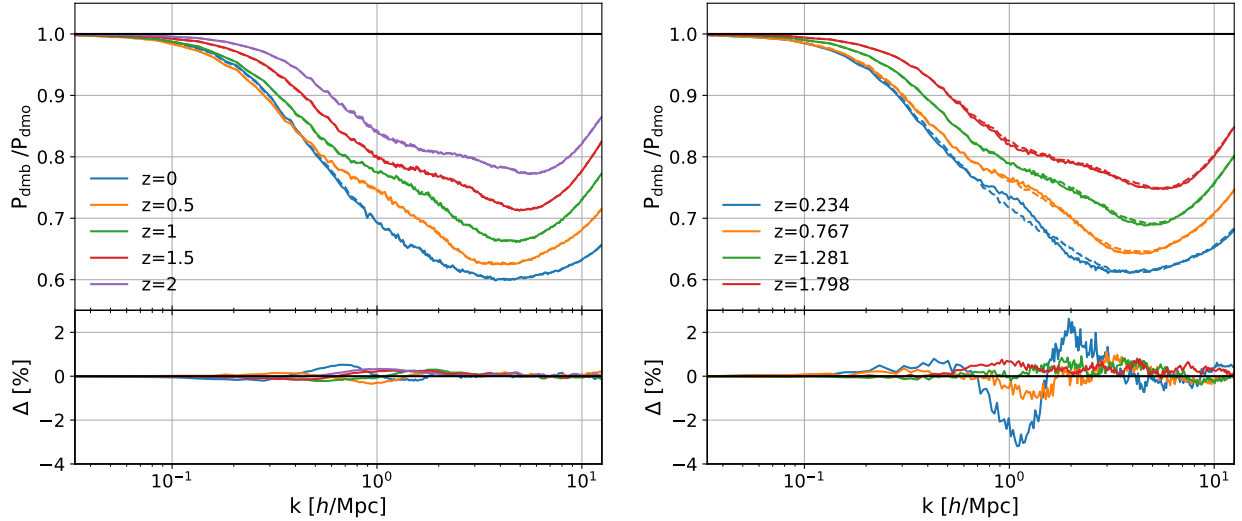


Figure 5: Results for the emulation of sample 1: $f_b = 0.171753000$, $\log_{10} M_c = 15.1972851$, $\mu = 0.938900789$, $\theta_{ej} = 5.10189264$, $\eta_{star} = 0.370061019$, and $\eta_{cga} = 0.555513395$.

In Fig.5 we see that the standard redshifts are accurately emulated within 0.5% error. The interpolated results seems also to be quite well described by the emulator within 1% error, except for the case with $z = 0.234$. By reducing the redshift the real power suppression presents an oscillation between $k = 0.5 \text{ h/Mpc}$ and $k = 5 \text{ h/Mpc}$ that is not described by the emulator in particular for the smallest interpolated redshift. Analogously to sample 0, also in this case we observe the strongest suppression $\sim 40\%$ at redshift $z = 0$.

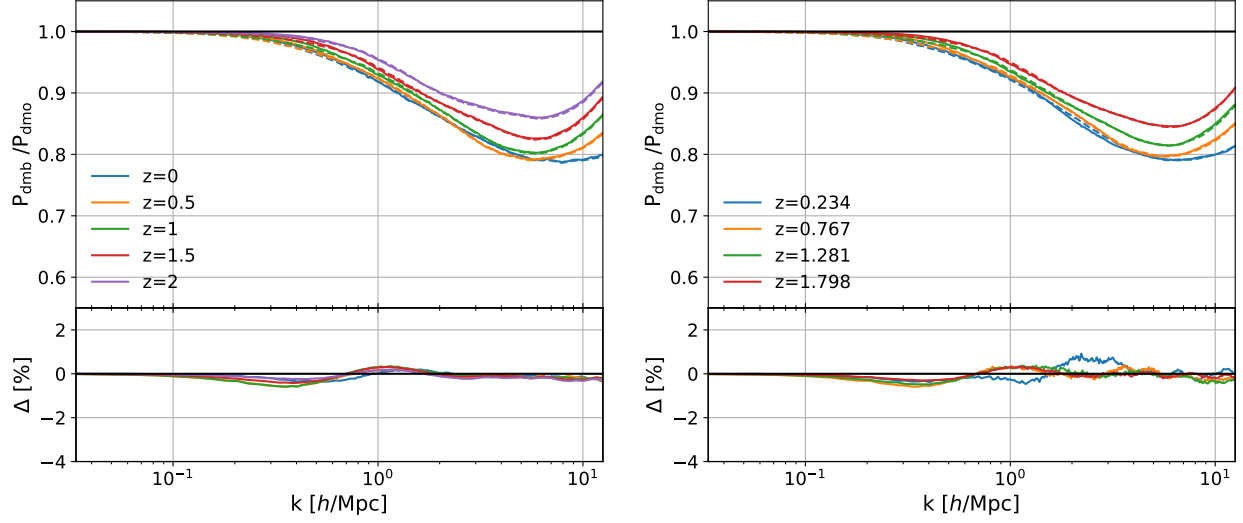


Figure 6: Results for the emulation of sample 2: $f_b = 0.131911086$, $\log_{10} M_c = 13.5288144$, $\mu = 0.339449947$, $\theta_{ej} = 6.60468011$, $\eta_{star} = 0.360097111$, and $\eta_{cga} = 0.624989236$.

The results at all redshifts for sample 2, presented in Fig.6, show a good agreement between real data and emulation with relative errors below 1%. This baryonic model leads to a smaller suppression in the order of 20%.

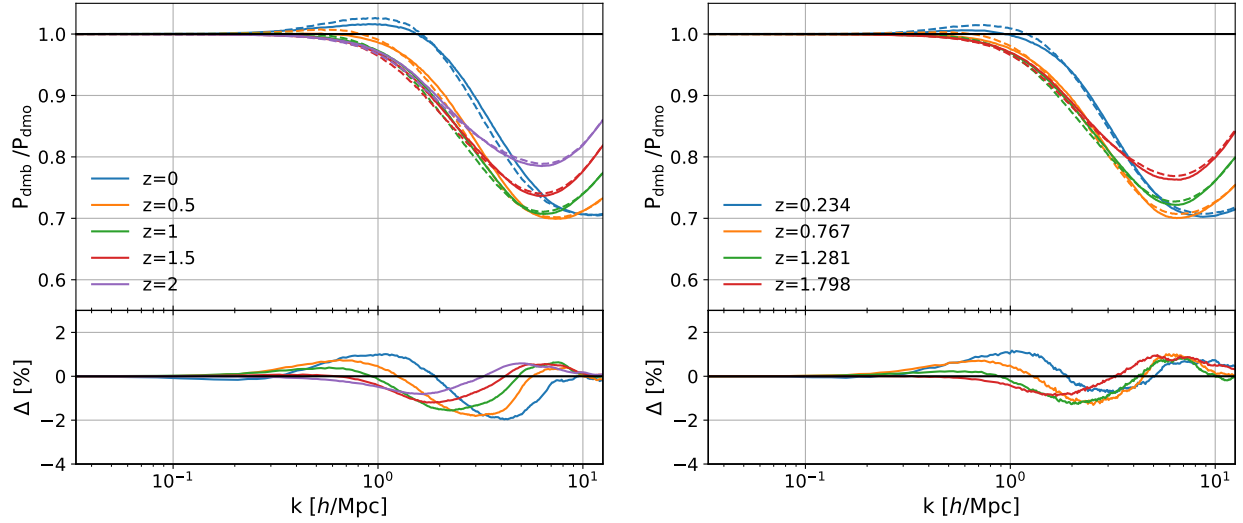


Figure 7: Results for the emulation of sample 3: $f_b = 0.185102187$, $\log_{10} M_c = 14.4185415$, $\mu = 0.498056100$, $\theta_{ej} = 2.00671323$, $\eta_{star} = 0.267163204$, and $\eta_{cga} = 0.679916413$.

The test point emulated in Fig.7 shows a maximum relative error around 2%. Moreover, in this case the emulation for the interpolated redshifts is better with respect to the standard case. This is the opposite of the expectation, from the fact that the linearly interpolated redshifts are based on the standard ones and so should in general be related to larger errors. The matter power spectrum suppression has its maximum at small redshifts and it is in the order of 30%.

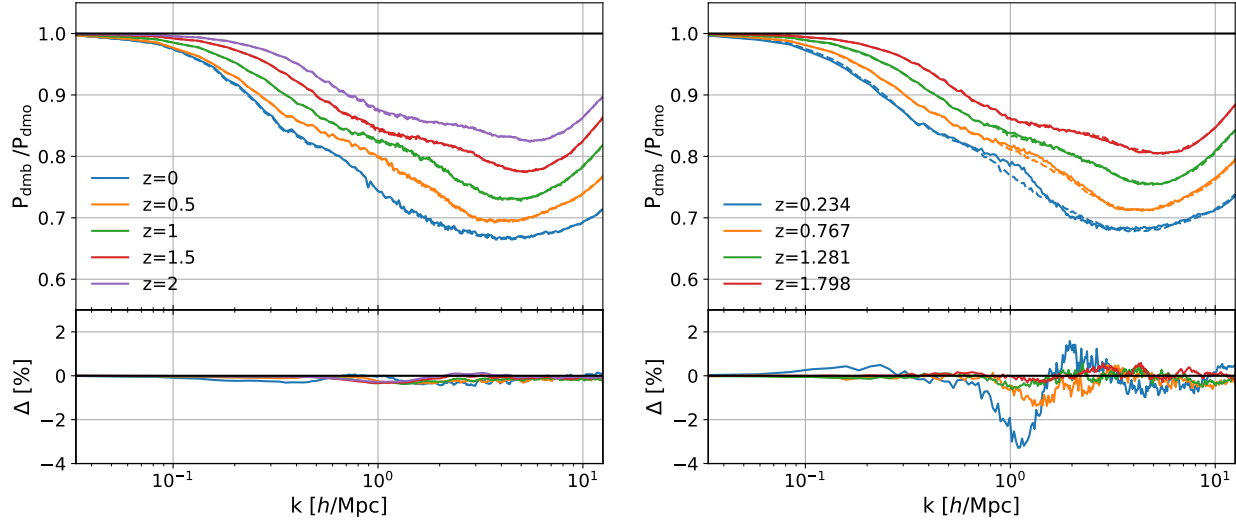


Figure 8: Results for the emulation of sample 4: $f_b = 0.149839396$, $\log_{10} M_c = 15.9845697$, $\mu = 0.797082016$, $\theta_{ej} = 7.35391483$, $\eta_{star} = 0.209096312$, and $\eta_{cga} = 0.637623288$.

In Fig.8 we observe the same behaviour as in Fig.5. The errors remains below 1%, except for the case $z = 0.234$ that presents a large oscillation of the power spectrum suppression. Also in this case, at redshift $z = 0$ we observe the maximum power suppression of $\sim 35\%$.

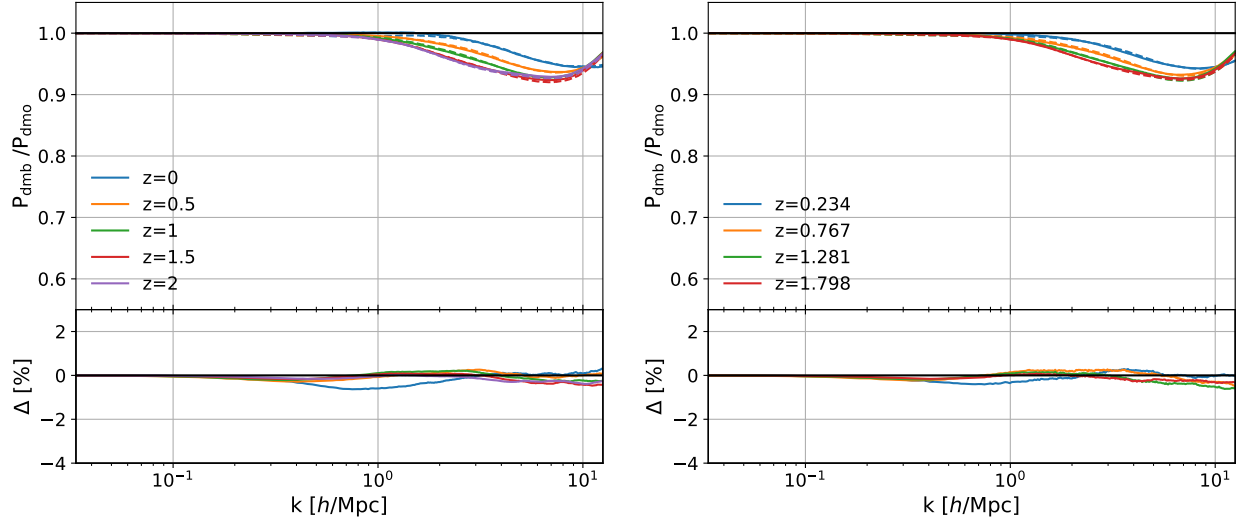


Figure 9: Results for the emulation of sample 5: $f_b = 0.162102650$, $\log_{10} M_c = 12.8009277$, $\mu = 0.582857882$, $\theta_{ej} = 4.13550454$, $\eta_{star} = 0.236488679$, and $\eta_{cga} = 0.531574004$.

The last test point, sample 5 presented in Fig.9, is precisely emulated within 1% error. We observe a power suppression smaller than 10% and an higher suppression for higher redshifts. This is in contrast with the results of the other samples.

From those figures we observe that each test point has a different shape and it is differently emulated. The first general conclusion that we get from those plots is that the emulator performs well within an error of 1–2% in most of the considered cases. On the other hand, there are some outlying results at some specific redshifts that are related to a worse performance within an error range of 2–3.5%.

In order to better understand the level of accuracy of our emulator, we can study the errors in two additional ways. The first way is to consider each redshift z separately. In Fig.10 we plot the relative error $(P_{emu}/P_{true} - 1)$ for the 9 considered redshifts values. Each panel of the figure represent the results of the

six test points evaluated on a specific redshift z . The maximum absolute error of our emulator, on the test set, is reached by sample 0 at $z = 0$ with a value $\max(P_{\text{emu}}/P_{\text{true}} - 1) = 3.296$. In terms of redshift, if we consider the maximum and the minimum errors, the case $z = 0.234$ is the worst emulated for which we get large errors for samples 0/1/4. On the other hand, the highest accuracy is reached at redshift $z = 2$, where all the samples are well described with absolute error below 1.512%. In terms of accuracy of the individual test points, except for redshift $z = 0.234$, the samples 1/2/4/5 are accurately emulated within 1% absolute error. Differently, as presented in Fig.10, samples 0 and 3 are overall worse described with largest errors around $k = 1 \text{ h/Mpc}$ and $k = 4 - 5 \text{ h/Mpc}$.

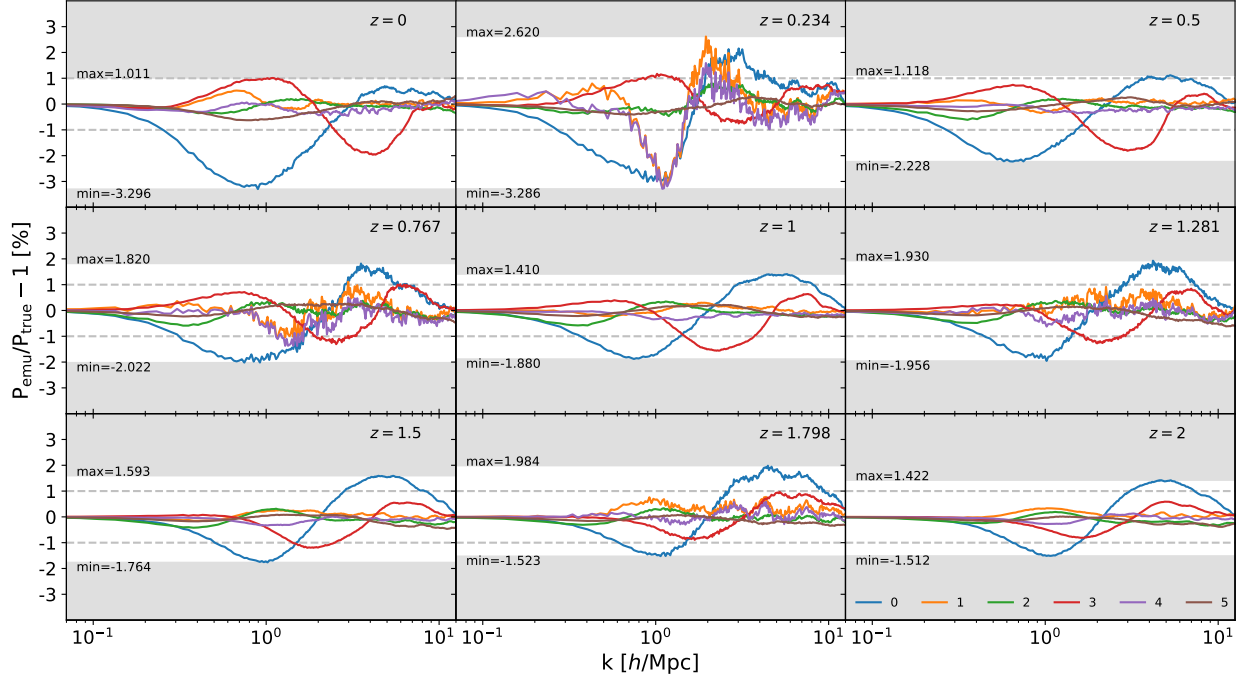


Figure 10: Relative error $P_{\text{emu}}/P_{\text{true}} - 1$ of the emulation on the 6 test points at different redshifts z . *Top from left:* redshifts $z = 0$, $z = 0.234$, and $z = 0.5$. *Centre from left:* redshifts $z = 0.767$, $z = 1$, and $z = 1.281$. *Bottom from left:* redshifts $z = 1.5$, $z = 1.798$, and $z = 2$. To each test sample a color is assigned. The dashed lines in each plot represent the $\pm 1\%$ error range. For each plot, the non-shaded region contains all the error curved and it is described with the maximum and the minimum relative error reached per redshift.

There is not a direct apparent correlation between the worse emulation of those samples and their location in the 6D - parameter space (see Table 3). This can be deduced from Fig.11, where the values of the free parameters are presented in a normalized range for each sample point. The only plausible explanation of this behaviour is that specific combinations of the model parameters f_b , $\log_{10}M_c$, μ , θ_{ej} , η_{star} , and η_{cga} lead to lower accuracy. In particular, sample 0 has f_b and $\log_{10}M_c$ very close to the upper boundaries and μ that is close to the lower one. Alternatively, sample 3 has θ_{ej} that is very close to the lower boundary, η_{cga} close to the upper boundary, and the other parameters spread around the center of the intervals. Nevertheless, also the other samples have parameter values lying in the neighbourhood of the boundaries, so we can not draw a concrete conclusion about the relation between emulation accuracy and 6D - spatial distribution of the parameters.

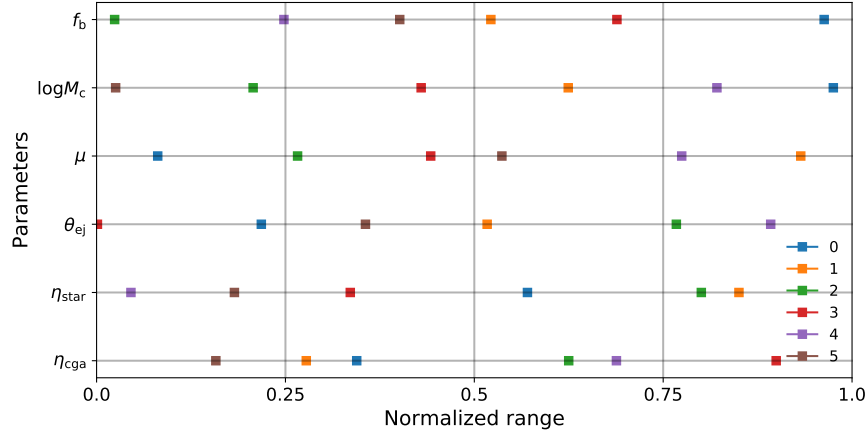


Figure 11: Distribution of the parameter values in the parameter ranges for each test sample. Different colors represent the different test points described in Table 3. The parameter values are normalized in order to be represented on a normalized x-axis that describes all the different ranges at once. The model parameters f_b , $\log_{10} M_c$, μ , θ_{ej} , η_{star} , and η_{cga} are plotted on the y-axis.

Figures 4-10 describe the performance of the emulator considering principally the maximum of the error, such that the best and the worst cases are defined according to it. This kind of error estimation depends on the size of the test set, i.e. to a larger test set would correspond a higher maximum error. In order to avoid this dependency on the test set size, we follow an alternative approach which is presented in Fig.12. We have 6 sample points and 9 studied redshifts, so in total we can count on 54 different emulations. For each of those emulation we have the relative error estimate for several k -values. Although our data set is composed only of 6 points, it is possible to study the error distribution. We divide the k -range in 20 logarithmically spaced k -bins. Each bin contains all the error values for the 54 cases available in the corresponding k -range. In the left plot of Fig.12 we plot a histogram for each k -bins that represents the distribution of the relative error $\Delta = P_{emu}/P_{true} - 1$. The aim of our emulator is obviously to be as accurate as possible, so with an error approaching zero. From the histograms plot we see that the histograms peak around this value. Nevertheless, this plot is not enough to quantify the emulation performance. So, we divide the errors for each bin in positive and negative values and we aim to calculate the one standard deviation -1σ – and the two standard deviation -2σ – regions. This gives us an estimate of the error margin that contains 68.27% and 95.45% respectively of the emulation errors. The results are presented in the right plot of Fig.12. As already seen when considering the figures 4-10, the worst performance is given on scales around $k = 1 h/\text{Mpc}$ and $k = 4 - 5 h/\text{Mpc}$. Around $k = 1 h/\text{Mpc}$ the 1σ -error reaches an absolute value about 1.5%, and the 2σ -error an absolute value around 3%. For the 1σ -significance, except for the near neighbourhood of this scale k , the emulator has good accuracy related to absolute errors smaller that 1%. At 2σ -significance, 95.45% of the emulator errors are restricted below a 2%-limit, except for the region around $k = 1 h/\text{Mpc}$ that has a maximum error of 3%.

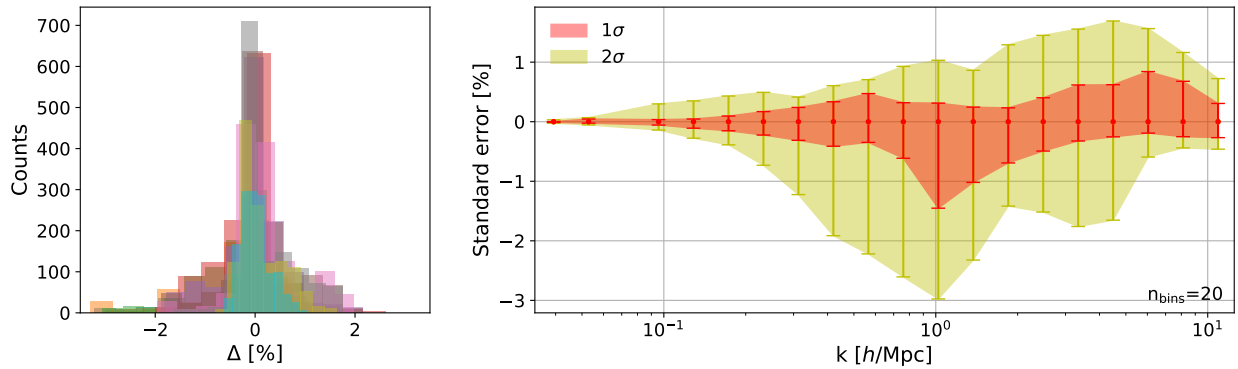


Figure 12: Left: histograms of the emulation errors $\Delta = P_{emu}/P_{true} - 1$ for each k -bin considered based on the results of 9 redshifts z . Right: 1σ - and 2σ -regions representing the standard error for the 20 logarithmically spaced k -bins.

A larger test data set would obviously ensure a higher confidence about the error of the estimation. Nevertheless, the estimation based on the six sample points gives us a consistent idea about the emulator performance. We conclude that the emulator performs accurately at large scales and within 2% at a $1 - 2\sigma$ level.

4 Baryonic corrections on the shear angular power spectrum $C(\ell)$

In this section we introduce a method to calculate the shear angular power spectrum $C(\ell)$ that accounts for baryonic corrections. This method is constructed by implementing our emulator for baryon effects into the integrated cosmological Boltzmann solver `PyCosmo` developed by Refregier et al. [3, 19].

In Section 4.1 we define the angular power spectrum $C(\ell)$ and introduce alternative models that account for the baryon feedback effects. Subsequently, we compare our baryonic corrected spectrum with the results of those models. In Section 4.2 we describe the power suppression of the angular power spectrum $C_{\text{dmb}}(\ell)/C_{\text{dmo}}(\ell)$ at medium and small cosmological scales.

4.1 $C(\ell)$ construction and comparison

In Section 4.1.1 we introduce the weak lensing shear angular power spectrum and we describe the implementation of our baryon effects emulator in its calculation. In Section 4.1.2 we define the reference baryonic models used for the comparison. In Section 4.1.3 we introduce an alternative model that account for the baryon physics at medium and small cosmological scales by introducing a bias described by a fitting function. In Section 4.1.4 we introduce another model for the same purpose that considers a modified halo-model that can be adapted to account for the effects of baryon feedback. In Section 4.1.5 we compare the results of the different methods.

4.1.1 Construction and implementation

The projected angular power spectrum of the weak lensing shear $C(\ell)$ is independent of the redshift z and so can be directly observed through weak lensing observations. Therefore, it is important to mimic the effects of the presence of baryons on this observable quantity because it can be compared and tested with real observations.

Relying on Section 5.2 in [23], we describe how the shear power spectrum is constructed from the matter power spectrum. According to the Limber approximation the angular power spectrum is

$$C(\ell) = \int_0^{\chi_{\text{H}}} \frac{g^2(\chi)}{\chi^2} P\left(\frac{\ell}{\chi}, z(\chi)\right) d\chi, \quad (17)$$

where χ represents the comoving distance

$$\chi(z) = \int_0^z \frac{cdz'}{H(z')} = \frac{c}{H_0} \int_0^z \frac{dz'}{[\Omega_{\text{m}}(1+z')^3 + 1 - \Omega_{\text{m}}]^{1/2}}, \quad (18)$$

$\chi_{\text{H}} = \chi(z = \infty)$ is the today's particle horizon, $P\left(k = \frac{\ell}{\chi}, z(\chi)\right)$ is the matter power spectrum at scale k and redshift z , and $g(\chi)$ are the lensing weights

$$g(\chi) = \frac{3\Omega_{\text{m}}}{2} \left(\frac{H_0}{c}\right)^2 (1+z(\chi)) \int_{\chi}^{\chi_{\text{H}}} n_{\text{s}}(z(\chi')) \frac{(\chi' - \chi)}{\chi'} \frac{dz}{d\chi'} d\chi'. \quad (19)$$

The latter depend on the galaxy redshift distribution $n_{\text{s}}(z)$ which we assume to be

$$n_{\text{s}}(z) = \frac{1}{2z_0^3} z^2 \exp\left(-\frac{z}{z_0}\right) \quad (20)$$

with $z_0 = 0.24$ [23].

The weak lensing angular power spectrum calculator implemented in `PyCosmo` [3, 19] is constructed following Eq. 17. We implement the *baryon effects emulator*, developed in Section 3, into the `PyCosmo` routine in order to generate an angular power spectrum that considers baryonic corrections. The new implementation requires the free parameters f_{b} , $\log_{10} M_{\text{c}}$, μ , θ_{ej} , η_{star} , and η_{cga} in order to emulate the matter power spectrum suppression.

The implementation of the baryonic corrections is straightforward using the constructed emulator. In order to calculate the corrected angular power spectrum $C_{\text{dmb}}(\ell)$, we replace the matter power spectrum

$P_{\text{dmo}}(k, z)$ in Eq.17 with the corrected matter power spectrum $P_{\text{dmb}}(k, z) = P_{\text{dmo}}(k, z)B(k, z)$, where $B(k, z)$ is the emulated power suppression. The latter is emulated at specific cosmological scales in the range $3.4 \times 10^{-2} h/\text{Mpc} \lesssim k \lesssim 12.5 h/\text{Mpc}$. However, in the integration in Eq.17, $k = \ell/\chi$ takes different values inside and outside this range. Therefore, we perform a linear interpolation for arbitrary k -values inside the range, and we perform a linear extrapolation at the end of the known data for arbitrary k -values outside.

4.1.2 Reference baryonic models

In order to test the results for the baryonic corrected angular power spectrum implemented in `PyCosmo`, we need reference baryonic models with fixed combinations of f_b , $\log_{10} M_c$, μ , θ_{ej} , η_{star} , and η_{cga} . The cosmological parameter $f_b = \Omega_b/\Omega_m$ is set by the choice of the standard cosmology introduced in Table 1. For the choice of the baryonic parameters we refer to the work of Schneider et al. [23]. According to stacked X-ray observations of gas density profiles (e.g. from *ROSAT*/*PSPC* and *XMM-Newton*), they derive a very conservative range of values for the gas ejection parameter, i.e. $\theta_{\text{ej}} \in [2, 8]$. Moreover, using observations of X-ray gas fractions, they constrain the parameters M_c and μ which describe the slope of the gas density profile as a function of halo mass. This method requires knowledge about the total halo mass contained into r_{500} , where r_{500} represents the radius where the mean halo density relative to the critical density of the Universe $\rho_{\text{crit}} = 3H^2/8\pi G$ is equal to 500. However, the measure of this quantity is affected by uncertainties related to the assumption of hydrostatic equilibrium. Therefore, Scheider et al. introduce a hydrostatic mass bias b_{hse} defined in Eq.4.3 in [23]. They consider three models related to different hydrostatic mass bias values. Model A assumes the hydrostatic mass to be correct ($1 - b_{\text{hse}} = 1.00$). Model B and C assume that the total mass in hydrostatic equilibrium is underestimated by 20% and 40% respectively with respect to the true halo mass ($1 - b_{\text{hse}} = 0.83$ for Model B and $1 - b_{\text{hse}} = 0.71$ for Model C). For each model they constrain M_c and μ by comparing the gas fraction from X-ray observations with the predictions of the baryonic correction model described in Section 2.1. In addition, they consider three gas ejections radii θ_{ej} , i.e. minimum (min) radius with $\theta_{\text{ej}} = 2.0$, best-guess (avg) radius $\theta_{\text{ej}} = 4.0$, and maximum (max) radius $\theta_{\text{ej}} = 8.0$.

Name	$1 - b_{\text{hse}}$	θ_{ej}	$M_c [\text{M}_\odot/h]$	μ
Model A-min	1.0	2	1.1×10^{15}	0.17
Model A-avg	1.0	4	2.3×10^{13}	0.31
Model A-max	1.0	8	8.1×10^{12}	0.59
Model B-min	0.833	2	1.2×10^{16}	0.14
Model B-avg	0.833	4	6.6×10^{13}	0.21
Model B-max	0.833	8	8.1×10^{12}	0.31
Model C-min	0.714	2	3.5×10^{16}	0.14
Model C-avg	0.714	4	1.9×10^{14}	0.17
Model C-max	0.714	8	8.1×10^{12}	0.21

Table 4: Models with best fitting parameters M_c and μ according to different assumptions on hydrostatic equilibrium described by parameter b_{hse} , and for different gas ejection radii θ_{ej} . The stellar parameters are fixed to $\eta_{\text{star}} = 0.32$ and $\eta_{\text{cga}} = 0.6$. Table referring to Table 2 in Schneider et al. [23].

Table 4, taken from the study of Schneider et al. [23], summarizes the best-fitting values for M_c and μ found for the 9 reference models. Model A-min and Model C-max are the most extreme cases according to their study. The models lying into the region in-between these extreme cases provide an estimate of current uncertainties for X-ray data. Based on those results we test our angular power spectrum calculator against alternative models described in Sections 4.1.3 and 4.1.4.

4.1.3 Fitting function for the baryon feedback effects

The first approach describes baryonic feedback models introduced by Harnois-Déraps et al. [5] obtained from the results of the Over- Whelmingly Large (OWL) Simulation Project [20, 26]. In particular, Ref. [5] introduce a fitting function that describes the baryon feedback bias $b_{\text{m}}^2(k, z)$ responsible for baryonic

corrections on the dark-matter-only matter power spectrum. The baryonic corrected matter power spectrum is then described by

$$P_{\text{dmb}}(k, z) = b_{\text{m}}^2(k, z)P_{\text{dmo}}(k, z) \quad (21)$$

where the bias $b_{\text{m}}^2(k, z)$ is described by the fitting function defined in Eq.10 in [5]:

$$b_{\text{m}}^2(k, z) = 1 - A_z e^{(B_z x - C_z)^3} + D_z x e^{E_z x} \quad (22)$$

with $x = \log_{10}(k/[h\text{Mpc}^{-1}])$. The terms A_z , B_z , C_z , D_z , and E_z depends on the redshift according to the relation $A_z = A_2/(1+z)^2 + A_1/(1+z) + A_0$. Table 2 in [5] describes the best-fitting parameters for different baryonic models. We are interested in the feedback from active galactic nuclei (AGN), therefore we consider the corresponding best-fitting parameters.

For the comparison with our implementation, we consider the work of Hikage et al. [6] and the work of Köhlinger et al. [10]. They describes baryonic corrections by implementing the fitting formula in Eq.22 with an additional baryon feedback amplitude A_{B} [6] (parametrized by A_{bary} in [10]) that regulates the strength of the baryon feedback effect

$$b_{\text{m}}^2(k, z) = 1 - A_{\text{B}} \left[A_z e^{(B_z x - C_z)^3} - D_z x e^{E_z x} \right]. \quad (23)$$

This free amplitude is constrained by flat priors. Especially, the amplitude is restricted to $A_{\text{B}} \in [-5, 5]$ in Hikage et al. [6], and to $A_{\text{B}} \in [0, 10]$ in Köhlinger et al. [10].

4.1.4 Modified halo-model accounting for baryon feedback effects

The second approach that we introduce is constructed on the modified halo-model from Mead et al. [16] and is constrained by the work of Hildebrandt et al. [7].

The principal consequence of baryon presence in haloes is the modification of their internal structure. Two main processes contribute to this modification. The gas cooling increases the density in the centre of haloes, whereas the haloes concentration is decreased by violent feedback, such as that from AGN. According to Mead et al. [16], in order to describe those baryonic processes, only two parameter are necessary. The minimum halo concentration A can be varied to capture the concentration increase during gas cooling (Eq.14 in [16]). The bloating parameter η_0 accounts for the bloating of halo profiles due to violent feedback (Eq.26 and 29 in [16]). As explained in Mead et al. [16], this two-parameter model can be reduced to a one-parameter model

$$\eta_0 = 1.03 - 0.11A \quad (24)$$

due to their degeneracy.

Hildebrandt et al. [7] impose a top-hat prior $A \in (2, 4)$ on the halo-concentration (parametrized with B in [7]). The prior has been constructed by considering the plausible feedback scenarios from the OWLS simulations.

4.1.5 Comparison of the baryonic models

We implement the methods defined in Sections 4.1.3 and 4.1.4 in PyCosmo such that we can generate the angular power spectrum $C(\ell)$ for a given baryon feedback amplitude A_{B} and respectively for a given halo-concentration A . In Fig.13 we compare the angular power spectrum generated according to those two methods with the results of the implementation of the *baryon effects emulator*.

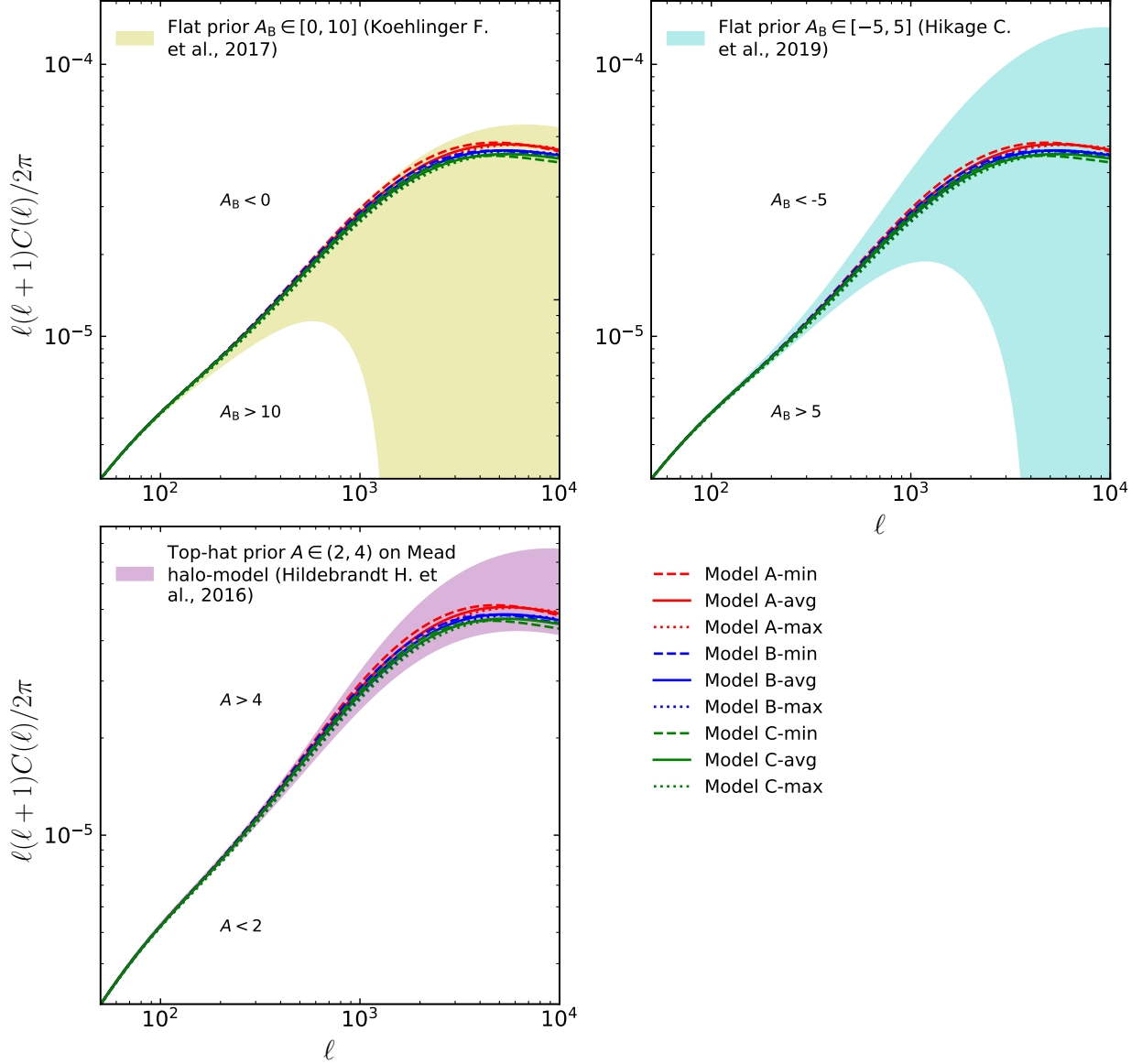


Figure 13: Figures representing the shear angular power spectrum $\ell(\ell+1)C(\ell)/2\pi$ plotted versus the multipole moments ℓ . *All:* using the implementation in `PyCosmo` of the baryonic correction developed in Section 3, we generate the angular power spectrum for the reference models described in Table 4. *Top left:* shaded region represents the plausible baryon feedback scenarios according to Köhlinger et al. [10] that assumes a flat prior $A_B \in [0, 10]$ (Section 4.1.3). *Top right:* shaded region represents the plausible baryon feedback scenarios according to Hikage et al. [6] that assumes a flat prior $A_B \in [-5, 5]$ (Section 4.1.3). *Bottom left:* shaded region represents the plausible baryon feedback scenarios given by the Mead halo-model [16] constrained with a top-hat prior on the halo-concentration $A \in (2, 4)$ according to the study of Hildebrandt et al. [7] (Section 4.1.4).

First consideration on Fig.13 comes from the comparison of $\ell(\ell+1)C(\ell)/2\pi$ generated with the baryonic correction model for the models described in Table 4, with the shaded regions from the other models. We see that our implementation (top left figure in Fig.13) gives tighter constraints on the plausible baryon feedback scenarios with respect to the priors defined by the other models. Probably, if we consider more extreme baryonic models than those described in Table 4, we would get a wider range of possible scenarios. Nevertheless, those additional models would not be in good agreement with the X-ray gas fractions observations considered by Schneider et al. [23], and so they could not be considered reliable as the reference ones chosen which give a physically motivated set of baryonic models.

Second consideration on the figure is that the emulation for the reference models always lies in the shaded regions given by the priors chosen in [6, 7, 10]. This is an important point worth noting because it means

that it is possible to reduce the prior-ranges due to baryonic effects by a lot if X-ray observations are included in the weak lensing analysis.

4.2 Power suppression of the angular power spectrum spectrum

Analogously to Section 2.2, where we describe the power suppression of the matter power spectrum at medium and small cosmological scales, in this chapter we probe the power suppression of the shear angular power spectrum $C(\ell)$ as a function of the multipole moments ℓ .

4.2.1 Angular power spectrum suppression for the reference models

We can define a suppression parameter $\tilde{B}(k, z) = C_{\text{dmb}}(\ell)/C_{\text{dmo}}(\ell)$ that represents the ratio of the baryonic corrected angular power spectrum, derived by means of PyCosmo with implemented baryonic corrections as introduced in Section 4.1, and the dark-matter-only angular spectrum also generated by means of PyCosmo.

We consider the relative effects of baryons on the reference baryonic models described in Table 4. We aim to reproduce Fig.10 from Schneider et al. [23] in order to consider similarities and differences between their calculation of the weak lensing angular shear power spectrum and our implementation of baryonic corrections. Throughout this section we refer to the work of Schneider et al. [23] as S19. By comparing our baryonic corrected spectrum presented in Fig.14 with S19 we can observe similarities and differences.

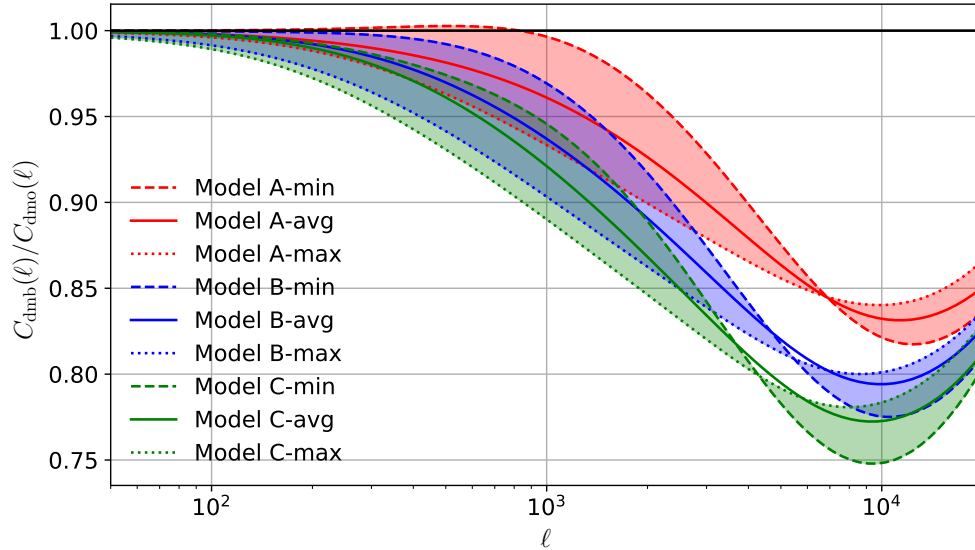


Figure 14: Suppression of the angular power spectrum $C_{\text{dmb}}(\ell)/C_{\text{dmo}}(\ell)$ due to baryon feedback effects. The power suppression is calculated for the 9 reference models exposed in Table 4. Those models are taken from the work of Schneider et al. [23]. The shaded regions, enclosed between the models with maximum gas ejection radius $\theta_{\text{ej}} = 8$ and minimum gas ejection radius $\theta_{\text{ej}} = 2$, represent the region where any realistic model is expected to lie.

The power suppression observed in Fig.14 has a similar shape compared to the results of the S19. The maximum suppression on the 9 models is reached around $\ell = 10^4$ (16 – 18% for model A, 20 – 22.5% for model B, and 22 – 25% for model C), whereas in the S19 those maxima are shifted to smaller multipole moments ℓ . This is a general difference between the two results, in fact they deviate significantly in terms of multipoles. An approximate comparison tells us that the curves deviate within 20 – 50% at medium and small cosmological scales. Moreover, we observe a larger power suppression with respect to the S19. In this respect, the curves agree to 5 – 10%.

Another evident difference is that, when moving to large multipole moments $\ell > 10^4$, the rate at which the power suppression decreases is much slower in Fig.14 compared to the results of the S19. Our results show a suppression decrease from $\ell = 10^4$ to $\ell = 2 \times 10^4$ of the order 2 – 7%. In the S19 we observe a much steeper decrease of the order of 10 – 15%. Assuming the results of S19 to be correct, one possible reason for

this difference could be the linear extrapolation used to calculate the baryonic power suppression outside of the emulation range (see Section 4.1.1).

For this comparison we assume the same cosmology and the same baryonic correction models used in S19. Therefore, we expect to find a good agreement with our implementation. As explained, this is not the case in particular for the shift along the ℓ -direction. We can not explain with confidence the reasons of these deviations, but we expose some possible explanations. First possible explanation is that the results of S19 are not correct and so the deviations can not quantify the accuracy of our method. Second possible explanation could be related to the emulation error described in Section 3.2. This uncertainty could rise due to the integration of the corrected matter power spectrum and lead to the observed deviations. The third possible explanation for the mismatch of the results could be related to the linear interpolation and the linear extrapolation used in order to calculate the integral defined in Eq.17. These techniques, described in Section 4.1.1, are approximation techniques which describe non-emulated physical regions and therefore they are probably related to additional errors.

4.2.2 Angular power spectrum suppression dependence on baryonic parameters

Section 3.1 of Schneider et al. [23] investigates the relation between the variation of the five baryonic parameters ($M_c, \mu, \theta_{ej}, \eta_{star}, \eta_{cga}$) and the suppression of the matter power spectrum. The main conclusion drawn is that the baryon suppression of the matter power spectrum is dominated by the gas parameters M_c and θ_{ej} . As explained in [23], this is a reasonable result because the baryonic suppression is dominated by AGN feedback mechanisms which control the amount of gas ejected into the intergalactic space.

We want to test if this relation is also observed for the suppression of the weak lensing shear angular power spectrum. In Fig.15 we study the suppression on the standard cosmology (see Table 1) for each emulation [17] by applying the standard baryonic correction model described in Table 2. In each subplot, except for the top-left one, we vary only one baryonic model parameter. In addition we also investigate the dependence of the suppression on the matter density Ω_m (top-left plot).

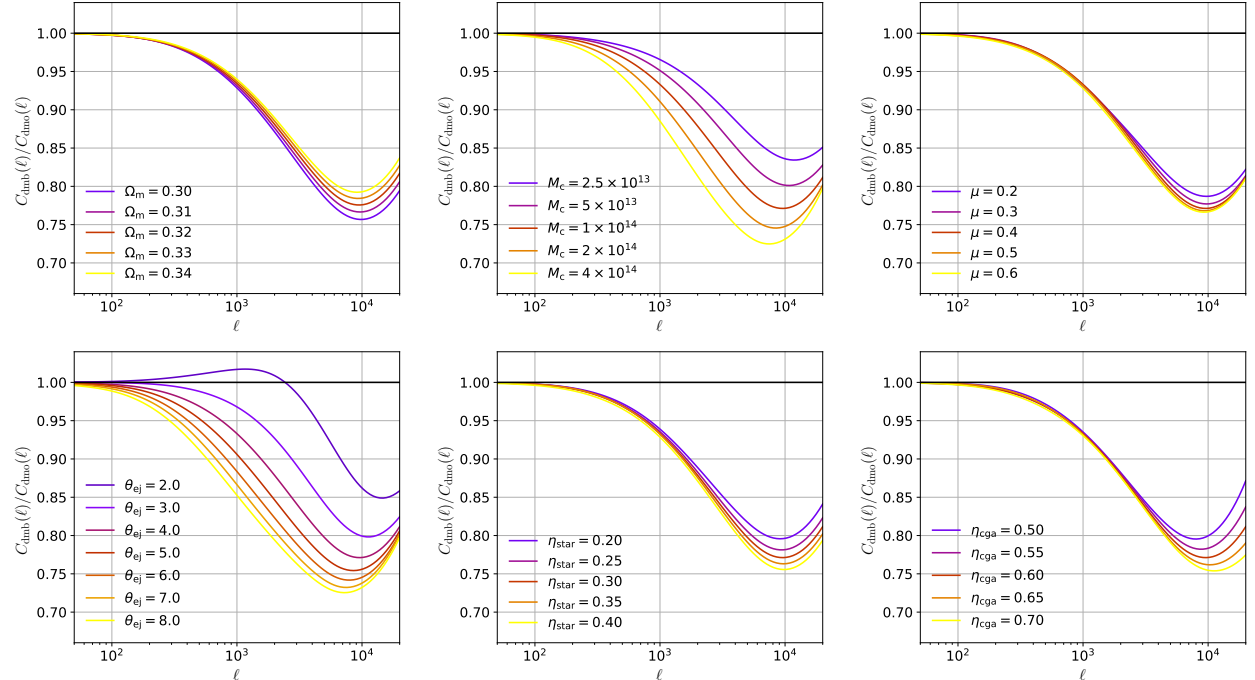


Figure 15: Dependence of the angular power spectrum suppression $C_{dmb}(\ell)/C_{dmo}(\ell)$ on matter density and baryonic parameters variations. The suppression is calculated on a standard cosmology described in Table 1. For each panel we vary only one model parameter of the standard baryonic correction model described in Table 2. *Top-left:* suppression for variable matter density Ω_m . *Top-centre:* suppression for variable gas parameter M_c . *Top-right:* suppression for variable gas parameter μ . *Bottom-left:* suppression for variable gas parameter θ_{ej} . *Bottom-centre:* suppression for variable stellar parameter η_{star} . *Bottom-right:* suppression for variable stellar parameter η_{cga} .

Fig.15 shows similar results as for the suppression of the matter power spectrum presented in [23]. The suppression of the angular power spectrum is driven by the gas parameters M_c and θ_{ej} (top-centre and bottom-left plots). Varying the μ parameter (top-right plot) has not a big impact on the magnitude of the suppression. The dependence on the stellar parameters η_{star} and η_{cga} (bottom-centre and bottom-right plots) is also weak and becomes distinguishable only for multipoles $\ell > 10^3$. On the other hand, also the dependence on the matter density Ω_m has not a large effect on the suppression of the spectrum (top-left plot). We observe that the amplitude of the suppression increases when the matter density is reduced, i.e. when the cosmic fraction f_b is enhanced due to fixed baryon density $\Omega_b h^2 = 0.0224$. This is not surprising since a larger cosmic fraction means that a larger portion of the total matter density is composed by baryons, and so their effect on the power spectrum is enhanced.

5 Conclusion

In this paper, we have considered the present-day problem of describing baryon feedback effects on the matter density distribution of the Universe. In this respect, we have presented an emulator [24] that mimics the baryonic corrections of the matter power spectrum and we have implemented it to calculate the projected angular power spectrum of the weak lensing shear.

The emulator is based on a metamodeling technique called polynomial chaos expansion [14] and it is constructed on a *baryonic correction model* [21, 23] which substitutes the dark-matter halo profiles with halo profiles that accounts for two additional components, i.e. gas and stars.

We have tested the dependence of the model on the cosmological parameters $(\Omega_m, \Omega_b, h, n_s, \sigma_8)$, and on the cosmic fraction f_b , and we have concluded that the model is in principle only sensible to variations of the cosmic fraction, when considering reasonable parameter values. Moreover, we have deduced that the power suppression varies less than 2% when the cosmological dependence is neglected in N -body simulations. This means that the power suppression is characterised mostly by the model and therefore only one reference N -body simulation can be used to test different cosmologies.

We have shown that the strength of the power suppression depends on the cosmic fraction f_b and on the baryonic parameters $(M_c, \mu, \theta_{ej}, \eta_{star}, \eta_{cga})$. In particular, we have shown that the power suppression of the angular power spectrum is very sensible to the variations of the gas parameters M_c and θ_{ej} (Fig.15).

We have tested the accuracy of our emulator with respect to the effective implementation of the *baryonic correction model*. In this respect, we have found that at 1σ -level the emulator performs within a 1.5% error margin, therefore representing a quite accurate estimator for the power suppression of the matter power spectrum. Moreover, its easy and fast implementation represents a great advantage in comparison to other methods.

The implementation of the emulator for the calculation of the projected angular power spectrum of the weak lensing shear gives us promising results. The main motivation behind its construction is to provide a tool for the cosmological parameter estimation. Compared to alternative methods [5, 6, 7, 10, 16], our method gives reasonable outcomes, empirically motivated by the comparison with X-rays observations of gas fractions described in [23]. According to these observations, our calculator for the angular power spectrum sets tighter constraints on the plausible baryon feedback scenarios.

The understanding of baryon feedback effects is of vital importance in order to restrict the systematical uncertainty related to current and future weak lensing surveys. The new tools presented in this paper, give us the opportunity to have a more accurate theoretical prediction on direct observables like the angular power spectrum from weak lensing observations. These tools can be implemented in order to perform a cosmological parameter estimate that can in principle bring reliable confirmations for or against the standard model of cosmology.

Acknowledgements

I thank Aurel Schneider for his support and availability throughout the thesis. I thank Mischa Knabenhans for his support related to the construction of the emulator. I thank Alexandre Refregier and Adam Amara for giving me the chance to perform my master thesis in the cosmology group.

References

- [1] Efron B., Hastie T., Johnstone I., Tibshirani R., 2004, *Least angle regression*, The Annals of Statistics, 32, 407
- [2] Euclid Collaboration, Knabenhans et al., 2018, *Euclid preparation: II. The EuclidEmulator - A tool to compute the cosmology dependence of the nonlinear matter power spectrum*, arXiv:1809.04695v2
- [3] ETH Zurich Cosmology Group, 2013, *PyCosmo documentation*. Retrieved from: <https://cosmo-docs.phys.ethz.ch/PyCosmo/>
- [4] Gill S.P.D., Knebe A., Gibson B.K., 2004, *The evolution of substructure - I. A new identification method*, MNRAS, 351, 399
- [5] Harnois-Déraps J., van Waerbeke L., Viola M., and Heymans C., 2015, *Baryons, neutrinos, feedback and weak gravitational lensing*, MNRAS 450, 1212-1223
- [6] Hikage et al., 2018, *Cosmology from cosmic shear power spectra with Subaru Hyper Suprime-Cam first-year data*, arXiv:1809.09148v1
- [7] Hildebrandt H. et al., 2016, *KiDS-450: Cosmological parameter constraints from tomographic weak gravitational lensing*, MNRAS 465, 1454-1498
- [8] Knabenhans M., 2018, *EuclidEmulator* GitHub repository, <https://github.com/miknab/EuclidEmulator>
- [9] Knollmann S.R., Knebe A., 2009, *AHF: AMIGA'S HALO FINDER*, ApJS, 182,608
- [10] Köhlinger F. et al., 2017, *KiDS-450: the tomographic weak lensing power spectrum and constraints on cosmological parameters*, MNRAS 471, 4412-4435
- [11] Lesgourgues J., 2011, *The Cosmic Linear Anisotropy Solving System (CLASS) I: Overview*, arXiv:1104.2932v2
- [12] Longair M.S., 2008, *Galaxy Formation*, Berlin: Springer
- [13] Marelli S., and Sudret B., *UQLab: A framework for uncertainty quantification in Matlab*, Proc. 2nd Int. Conf. on Vulnerability, Risk Analysis and Management (ICVRAM2014), Liverpool, United Kingdom, 2014, 2554-2563.
- [14] Marelli S., Sudret B., 2017, Technical report, *UQLab user manual - Polynomial Chaos Expansion*. Chair of Risk, Safety & Uncertainty Quantification, ETH Zurich, Zurich, doi:10.13140/RG.2.1.3778.7366
- [15] McKay M.D., Beckman R.J., and Conove W.J., 1979, *Comparison of Three Methods for Selecting Values of Input Variables in the Analysis of Output from a Computer Code*, doi: 10.1080/00401706.1979.10489755
- [16] Mead A. J. , Peacock J. A., Heymans C., Joudaki S., and Heavens A. F., 2015, *An accurate halo model for fitting non-linear cosmological power spectra and baryonic feedback models*, MNRAS, 454, 1958
- [17] Planck Collaboration, Aghanim et al., 2018, *Planck 2018 results. VI. Cosmological parameters*, arXiv:1807.06209v1

- [18] Potter D., Stadel J., and Teyssier R., 2016, *PKDGRAV3: Beyond Trillion Particle Cosmological Simulations for the Next Era of Galaxy Surveys*, arXiv:1609.08621v1
- [19] Refregier A., Gamper L., Amara A., and Heisenberg L., 2017, *PyCosmo: An Integrated Cosmological Boltzmann Solver*, arXiv:1708.05177v1
- [20] Schaye J. et al., 2010, *The physics driving the cosmic star formation history*, MNRAS, 402, 1536
- [21] Schneider A. and Teyssier R., 2016, *A new method to quantify the effects of baryons on the matter power spectrum*, arXiv:1510.06034v2
- [22] Schneider A., 2018, *corforb*, PyPI repository, <https://pypi.org/project/corforb/>
- [23] Schneider A., Teyssier R., Stadel J., Chisari N.E., Le Brun A.M.C., Amara A., and Refregier A., 2018, *Quantifying baryon effects on the matter power spectrum and the weak lensing shear correlation*, arXiv:1810.08629v2
- [24] Stoira N., 2019, *BaryonEffectsEmulator* GitHub repository, <https://github.com/nicolastoira/BaryonEffectsEmulator>
- [25] Tang B., 1993, *Orthogonal Array-Based Latin Hypercubes*, Journal of the American Statistical Association, 88, 1392
- [26] van Daalen M.P., Schaye J., Booth C.M., and Dalla Vecchia C., 2011, *The effects of galaxy formation on the matter power spectrum: a challenge for precision cosmology*, MNRAS, 415, 3649
- [27] Wambsganss J., 1998, *Gravitational Lensing in Astronomy*, arXiv:astro-ph/9812021v1